Full length article

On the competition in phase formation during the crystallisation of Al-Ni-Y metallic glasses

M.J. Styles [a, *], W.W. Sun [b], D.R. East [a], J.A. Kimpton [c], M.A. Gibson [a, b], C.R. Hutchinson [b]

[a] CSIRO Manufacturing, Clayton, 3168, VIC, Australia
[b] Department of Materials Science and Engineering, Monash University, Clayton, 3800, VIC, Australia
[c] Australian Synchrotron, Clayton, 3168, VIC, Australia

ABSTRACT

Glassy metals exhibit a range of interesting properties including high strength and corrosion resistance, but often have poor toughness and tensile ductility in the fully amorphous state. It has been shown that combinations of desirable properties can be achieved by the partial crystallisation of glass-forming alloys, either during controlled solidification or by annealing a fully amorphous glass. The aim of this investigation is to understand the competition in phase formation during the crystallisation of metallic glasses in the Al-Ni-Y system. High-resolution, *in situ* synchrotron powder diffraction has been used to quantitatively follow the evolution of phases in 5 different alloys between $Al_{87}Ni_9Y_4$ and $Al_{75}Ni_{15}Y_{10}$, as they were continuously heated to melting and subsequently cooled back to ambient temperature. Upon heating, the first crystallisation product was found to vary from FCC Al to the intermetallic Al_9Ni_2 phase with increasing Ni concentration. In addition, the crystallisation sequence also changed from a two-stage to a three-stage process. High number densities of crystallites ($\sim 10^{23}$ m^{-3}) were observed initially for both FCC Al and Al_9Ni_2. Upon cooling, the partially disordered Al_9Ni_3Y phase was found to form preferentially over the intermetallic phases observed during heating. The difference in competition in phase formation during heating and cooling are discussed in terms of nucleation barriers calculated using a recent thermodynamic assessment of the Al-Ni-Y system. The role of compositional heterogeneities in the as-quenched glasses and long-range diffusion on the nucleation process is discussed.

Crown Copyright © 2016 Published by Elsevier Ltd on behalf of Acta Materialia Inc. All rights reserved.

1. Introduction

If a liquid metal alloy is cooled at a sufficiently high rate it is possible to kinetically constrain the crystallisation process and obtain a glass devoid of long range order [1—4]. Metallic glasses have been studied in the laboratory since the 1960's [5,6]. Since that time, compositions have been developed which allow slower and slower cooling rates to be used so that bulk glassy materials may now be obtained with section sizes greater than 1 cm with cooling rates of around 1 K/s [7,8].

Glassy metals exhibit a range of interesting properties that make them promising for engineering applications. The absence of dislocations leads to strengths significantly greater than their crystalline counterparts [9,10]. Al- and Mg-based metallic glasses can exhibit strengths of 1—2 GPa [11—17], and Fe-based glasses have

been shown to have strengths of 3—4 GPa [18,19]. This is at least a factor of 2 higher than the best crystalline counterparts. Correspondingly, these glasses exhibit large elastic strain limits (~2%) [2,9,10] which, when combined with their high strengths, leads to the best known elastic energy storage properties (σ^2/E) of all metallic materials [20]. The absence of grain boundaries (and associated segregations and precipitations) can lead to considerable improvements in corrosion resistance [21—23], even in materials such as Mg which exhibit poor corrosion properties in crystalline form under most circumstances [24,25]. The absence of a liquid-to-crystal solidification process removes a large source of shrinkage in casting and consequently glassy metals have excellent dimensional casting tolerances [26]. Some glassy metals can be superplastically formed at temperatures between the glass transition (T_g) and the crystallisation temperature, in the same way that thermoplastic polymers are processed, potentially allowing the use of cheap, fast and flexible forming operations [26,27]. This collection of desirable properties have led metallic glasses from laboratory-scale fundamental interest to an engineering material

* Corresponding author.
E-mail address: Mark.Styles@csiro.au (M.J. Styles).

currently used in applications such as high frequency transformer cores (Fe-based glasses) [28], sensors (Co- and Fe-based glasses) [29], electronic device casings (Cu- and Zr-based glasses) [26], sporting goods (Zr-based glasses) [30], and many more potential uses [31].

One of the main weaknesses of metallic glasses is generally considered to be their limited fracture toughness and tensile ductility [32,33] which has impeded exploitation of their excellent strength and corrosion resistance as structural materials. However, recent advances in the development of glass/crystalline composites have led to glassy metals with much improved ductility and toughness [34—36]. There are a number of ways of fabricating glass/crystalline composites but one of the approaches involves controlling the partial crystallisation of the glass, either during cooling from the melt, or by controlled annealing of a fully amorphous precursor [37]. The addition of a crystalline phase into the glassy matrix has been shown, in some circumstances, to improve the ductility of the material by homogenising the spatial distribution of plasticity [38], but also in other cases improvements in strength [14,15], corrosion resistance [23], and soft magnetic properties [39—41] can also be obtained. Achievement of these improvements requires careful control over the size, shape, volume fraction and identity of the crystalline phases formed in the glassy matrix.

This brings to the forefront the central role that the kinetics of crystallisation plays in forming metallic glasses, and subsequent partial crystallisation for the improvement of properties. For these reasons, understanding the thermodynamics and kinetics of crystallisation of the supercooled liquid and glassy states has been a focus of significant research [42—45] and is the topic of this contribution.

The best glass forming compositions obviously exhibit slow crystallisation from the liquid during cooling (e.g. Zr-based Vitreloy alloys [7,46]). Al-based metallic glasses were not discovered until 1988 [11,47] and one of the factors which contributed to the delay is that crystallisation occurs relatively quickly in Al-based materials [48], meaning that fast cooling rates and fine-tuned alloy compositions are required to obtain glassy Al. Al-based glasses potentially provide an interesting strong, corrosion resistant and light weight material, and understanding the crystallisation of these marginal glass forming materials is one route toward understanding their comparatively poor glass formability. Some of the better known Al-based metallic glasses are based on Al-TM-RE systems, such as Al-Ni-Y [49] and Al-Fe-Y [50]. There have been a number of studies examining the glass formability of these compositions [51], crystallisation during annealing [52,53], as well as the mechanical [14,15] and electrochemical properties that result [23,54,55].

Of particular interest in Al-based glassy alloys is the observation that partial crystallisation of an initially glassy matrix is capable of forming a nanoscale distribution of FCC α-Al crystals. The nanoscale distribution of α-Al that forms can have number densities of the order of ~10^{23} m^{-3} [56] indicating a high nucleation rate and a slow growth rate. It is tempting to directly link this high crystal nucleation rate during the annealing of glassy Al matrices with the marginal glass formability of these Al-rich compositions. However, Vitreloy 1, which has outstanding glass formability, indicating sluggish crystallisation from the liquid during cooling [57], can also be annealed at relatively low temperatures and lead to a nanoscale distribution of FCC crystals with a similarly high number density [58]. Such high nucleation rates in Vitreloy 1 would seem inconsistent with the sluggish crystallisation kinetics from the liquid during cooling, and indicates that nucleation from the supercooled liquid is not necessarily the same as that from a glassy matrix.

There has been much interest in identifying the origin of the high nucleation rates observed during annealing of glassy matrices at low temperature [56,59,60]. In the case of Vitreloy 1, these high

rates cannot be rationalised by classical nucleation theory (CNT) [58]. In the context of Al-based glasses, the mechanisms responsible for the high nucleation rates of α-Al crystals are important for controlling the crystallisation nanostructure to optimise the possible improvements in the properties. It has been suggested that the supercooled Al liquid may undergo phase separation prior to the nucleation of the α-Al crystals [61—63] and that the nucleation occurs heterogeneously at the interfaces between the phase separating regions [64]. Other authors have suggested there exist in the as-quenched glassy matrix pre-existing α-Al nuclei [59,65—67] or other forms of medium range order (MRO) [68], and that these simply grow during annealing [66]. There is some evidence to suggest that both phase separation and Al-rich nano-regions can co-exist with different length scales [69]. It has also been emphasised that since the phases forming during crystallisation have substantially different chemistries to the matrix, the role of long range diffusion in nucleation must also be considered, e.g. the 'coupled-flux' model [59,70—72], and hence the calculations using CNT should not be expected to be quantitatively accurate.

In this study we quantitatively characterise the kinetics of crystallisation of a systematic series of Al-Ni-Y glassy alloys with increasing Ni content using *in situ*, high-resolution synchrotron powder diffraction. The crystallisation sequence is such that over the range of Ni contents examined, we sample a transition in the identity of the phase first appearing from FCC α-Al at low Ni contents, to Ni containing intermetallic phases (Al$_9$Ni$_2$ and Al$_3$Ni) at higher Ni contents. The competition in phase formation as a function of temperature and glass composition is clarified. We use a recent thermodynamic description of the Al-Ni-Y system [73,74] to compare the identity of the first phase observed experimentally during crystallisation with that expected from computational thermodynamic calculations of nucleation barriers. Estimates of the interfacial energy are made using a broken-bond model [75]. Examining this comparison, as a function of bulk Ni composition for a range of glassy alloys, allows some inferences to be made regarding the likely role of the different hypotheses (phase separation [61—64], pre-existing nuclei [59,65—67], coupled-flux models [70—72], etc.) responsible for the high nucleation rates observed in these alloys during crystallisation.

2. Experimental procedure

2.1. Materials and heat treatments

Melt spinning was used to prepare foil specimens of Al$_{87}$Ni$_9$Y$_4$, Al$_{86}$Ni$_{10}$Y$_4$, Al$_{83}$Ni$_{13}$Y$_4$, Al$_{81}$Ni$_{15}$Y$_4$, and Al$_{75}$Ni$_{15}$Y$_{10}$ (at%) using a substrate velocity of ~50 m/s and a cooling rate of ~2 × 10^6 K/s. This process resulted in ribbons with a thickness of ~20 μm and a width of ~1 cm. No further heat treatments were performed prior to the synchrotron experiment.

A chemical analysis was performed using ICP-AES on the alloys and the results are summarised in Table 1. The compositions of the as-spun materials were very close to the nominal alloy compositions. Minor amounts of impurity elements were also detected,

Table 1
Composition of the five alloy samples measured using the ICP-AES method, with the exception of oxygen, which was measured by inert gas fusion.

Sample	Al	Ni	Y	Cu	Fe	Si	Ta	O
Al$_{87}$Ni$_9$Y$_4$	Bal	9.426	4.136	0.006	0.010	0.040	0.012	0.132
Al$_{86}$Ni$_{10}$Y$_4$	Bal	10.716	4.111	0.003	0.009	0.029	0.011	0.165
Al$_{83}$Ni$_{13}$Y$_4$	Bal	13.856	4.040	0.011	0.009	0.025	0.012	0.159
Al$_{81}$Ni$_{15}$Y$_4$	Bal	15.592	3.986	0.004	0.009	0.020	0.012	0.129
Al$_{75}$Ni$_{15}$Y$_{10}$	Bal	15.809	9.964	0.013	0.011	0.024	0.025	0.274

however, with the exception of Ta, these elements did not have an observable effect on the crystallisation products.

2.2. In situ synchrotron X-ray powder diffraction

High-resolution X-ray powder diffraction patterns were collected using the Powder Diffraction beamline [76] at the Australian Synchrotron. A monochromatic X-ray beam with a nominal energy of 15 keV was used, and data were collected over the angular range 5–85.5° 2θ using the Mythen curved position sensitive detector [77]. The foils were cut into numerous fine strips, which were sealed (in air) into small diameter (0.7 mm) quartz capillaries and studied in Debye-Scherrer geometry [78]. The capillaries were continuously rotated about their axes at ~1 Hz in order to improve the particle statistics and hence help ensure accurate observed relative peak intensities. A precise determination of the X-ray wavelength (λ = 0.825953 Å), was derived from diffraction patterns collected from a sample of LaB_6 (NIST SRM 660b) mixed with diamond powder. For the purposes of visualising the data, the diffraction patterns, which were acquired in pairs with the detector offset by 0.5° 2θ, were merged using the program CONVAS2 [79] in order to eliminate the gaps between the modules of the Mythen detector. However, during the data analysis, the unmerged diffraction patterns were modelled independently to improve the effective time/temperature resolution.

The samples, contained within quartz capillaries, were heated using a hot-air blower at a constant rate of 10 °C/min up to ~840 °C (sufficient to form liquid in all the compositions studied), and subsequently cooled to 350 °C at the same rate before switching off the hot-air blower. The temperature was controlled by a thermocouple placed between the nozzle of the hot-air blower and the sample capillary. The sample temperature was calibrated using the known phase transition (solid-solid and solid-liquid) temperatures of a range of standard materials, including KNO_3, Ag_2SO_4, SiO_2 and KCl. After optimising the position of the hot-air blower relative to the sample capillary, the phase transitions in these standard materials were observed to occur over a 15 °C window, providing an estimate of the error in the sample temperature (±7.5 °C). In situ diffraction patterns were collected every 30 s for the duration of the heating cycle. No oxidation of the samples was observed in the XRD patterns at any stage, indicating that the sealing within quartz tubes was sufficient for the purposes of this experiment.

2.3. Powder diffraction data analysis

The in situ powder diffraction data were analysed by the Rietveld method [80], as implemented in the software package TOPAS (version 5, Bruker AXS). An empirical model for the instrument contribution to the peak shape was derived from patterns collected from standard materials (Y_2O_3 and LaB_6). The scattering from an empty capillary was modelled using a set of individual pseudo-Voigt peaks combined with a constant background. The widths of the pseudo-Voigt peaks were then fixed, and the relative intensities locked to a single scaling factor, allowing the signal from the capillaries in all subsequent data sets to be modelled using only two refinable parameters, i.e. a constant background and the capillary scaling parameter. In a similar fashion, the scattering from the glassy phase (at room temperature) of each alloy was modelled using a series of individual pseudo-Voigt peaks, the relative intensities of which were also locked to a single scaling factor (I_{Glass}). This approach allows the contribution of the capillary and the amorphous alloy to be distinguished, and provides a measure of the integrated intensity of the amorphous phase, which can then be used to assist the quantitative phase analysis. The remaining crystalline phases were modelled using known crystal structures.

The most widely used method for quantifying the phases present in a powder diffraction sample is the Hill-Howard algorithm [81], which calculates the relative phase fractions via the following equation:

$$W_\alpha = \frac{S_\alpha (ZMV)_\alpha}{\sum\limits_i S_i (ZMV)_i} \tag{1}$$

where W_α is the weight fraction of phase α, and S_i, Z_i, M_i and V_i are the Rietveld scale factor, the number of formula units per unit cell, the mass of the formula unit and the volume of the unit cell of phase i, respectively. However, this method will only provide absolute phase fractions if the material is entirely crystalline, and if all of the crystalline phases are accounted for in the analysis. This is a problem for glassy alloys.

An alternative method has been proposed by O'Connor and Raven [82] (summarised by Madsen and Scarlett [83]), which makes use of an overall instrument constant K:

$$W_\alpha = \frac{S_\alpha (ZMV)_\alpha \mu_m^*}{K} \tag{2}$$

where μ_m^* is the mass absorption coefficient of the sample. The constant K depends on a range of factors, including the intensity of the beam, the acquisition time, the volume of material illuminated, etc. Typically, the value for K is determined for a particular instrument configuration using a standard, highly crystalline material, and subsequently used to evaluate the phase fractions, including any amorphous component, in the sample of interest. For this reason, the O'Connor and Raven method is also known as the external standard approach. However, it can be difficult to apply this method to Debye-Scherrer geometry, due to the uncertainty regarding the precise size and packing density of each capillary, which affects the volume of material in the beam. This is particularly true for the amorphous alloy foils, which were cut into strips rather than crushed into a fine powder.

In this investigation, a modified version of the O'Connor and Raven method has been used to calculate the absolute phase fractions. Typically, K is evaluated by:

$$K = \frac{\mu_m^* \sum\limits_i S_i (ZMV)_i}{\sum\limits_i W_i} \tag{3}$$

where W_i is the known (absolute) weight fraction of crystalline phase i. If the sample is temporarily assumed to be completely crystalline when analysing each diffraction pattern j (where $j = 1$ to n), the weight fractions W_i sum to unity and a local estimate for K can be obtained for each data set from:

$$K_j = \mu_m^* \sum\limits_i S_{i,j} (ZMV)_{i,j} \tag{4}$$

If the mass and composition of the material in the beam is constant throughout the experiment (as it is here), μ_m^* is constant for all datasets. Therefore, as the crystallinity of the sample evolves over time, K_j will increase and decrease in proportion to the sum of the Rietveld scale factors, and reach a maximum when the sample is most crystalline. If, and only if, the sample can be assumed to be completely crystalline at this point, K_j is equivalent to the instrument constant K for a given sample. However, in order to account for any variations in the beam intensity and acquisition time, it is also necessary to normalise the scale factors ($S_{i,j}$) to the incident beam monitor counts (C_j) recorded for each diffraction pattern. Hence, for the conditions encountered in this experiment, K can be

expressed as:

$$K = \max_{j=1\to n}(K_j) = \mu_m^* \max_{j=1\to n}\left(\frac{1}{C_j}\sum_i S_{i,j}(ZMV)_{i,j}\right) \quad (5)$$

The absolute phase fractions in a given sample can then be calculated using:

$$W_{\alpha,j} = \frac{\frac{S_{\alpha,j}}{C_j}(ZMV)_{\alpha,j}}{\max_{j=1\to n}\left(\frac{1}{C_j}\sum_i S_{i,j}(ZMV)_{i,j}\right)} \quad (6)$$

The validity of this approach is discussed in Section 3.

This approach allows us to quantitatively monitor both the identity and fraction of each phase forming in the glassy matrix during crystallisation. Estimates can also be made for the size of the crystallites based on the diffraction peak profiles, which, when combined with the fractions transformed, allows an estimate of the number density of crystals to be made. As will be shown, number densities of ~10^{23} m^{-3} are reached not only for the FCC α-Al forming from the matrix (consistent with previous studies [56,64,84]), but also for the intermetallic phases appearing in the higher Ni containing compositions.

Finally, it should be noted that the errors reported for the parameters determined by Rietveld analysis are two times the estimated standard deviations (i.e. 2σ) calculated by Topas, and will underestimate the true errors in the measurements [85]. These so-called "Rietveld errors" are based on the numerical fit to the data, and are provided to give an impression of the stability of the refined parameters.

2.4. Transmission electron microscopy (TEM)

To complement the *in situ* XRD studies, a sample of the Al$_{87}$Ni$_9$Y$_4$ alloy, heated at a rate of 10 °C/min to ~340 °C and then cooled to room temperature, was examined using transmission electron microscopy. The TEM foil was prepared by electro-polishing using a nitric acid-methanal electrolyte at ~30 °C, followed by plasma cleaning. The sample was examined using a Tecnei F20 field emission gun (FEG) TEM operating at 200 kV. Imaging was performed in bright field (BF) and high angle annular dark field (HAADF) modes. Energy dispersive spectroscopy (EDS) was used to map the nanostructure and point analysis was performed to measure the compositions inherited by the growing phases.

2.5. Small angle X-ray scattering (SAXS)

One of the hypotheses to explain the high nucleation rates of α-Al crystals observed in glassy Al alloys is the presence of heterogeneities in the as-spun materials. These may be a result of phase separation, quenched in Al rich regions, or other forms of MRO. Small angle X-ray scattering (SAXS) measurements were performed on samples of the as-spun ribbons to provide insight into the possible presence of any significant chemical heterogeneities on length scales consistent with the high number density of α-Al crystallites observed. SAXS is sensitive to variations in electron density in a material and therefore Al-rich regions will show a SAXS contrast with the surrounding matrix. The SAXS measurements were performed using a laboratory Bruker N8 SAXS instrument, employing a Cu microfocus source operating at 50 kV and 1 mA. Data were acquired from single layers of as-spun foil (~20 μm thick), for 30 min. The data were collected with a 2D detector allowing access to a scattering vector (q) range from ~0.01 to 0.38 Å^{-1}. The resulting patterns were isotropic and were background

subtracted and presented in the form of azimuthally averaged intensity, I, as a function of q.

3. Results

3.1. Al$_{87}$Ni$_9$Y$_4$ heated at 10 °C/min

An overview of the diffraction patterns observed during the *in situ* heating of the Al$_{87}$Ni$_9$Y$_4$ alloy is shown in Fig. 1, which reveals a two-stage crystallisation process prior to melting. The sample is initially fully amorphous with no crystalline peaks evident in the diffraction patterns. As the sample is heated above 180 °C, the FCC α-Al phase begins to form. The α-Al peaks are initially quite broad, indicating a small crystallite size, but grow in intensity and narrow in width as the temperature increases. The second stage of crystallisation occurs as the sample is heated above 347 °C, when the Al$_3$Ni [86] and Al$_{19}$Ni$_5$Y$_3$ [52,87] phases appear simultaneously. The width of the α-Al peaks narrow quickly as Al$_3$Ni and Al$_{19}$Ni$_5$Y$_3$ form, indicating a rapid increase in crystallite size. At ~700 °C the sample begins to melt and the intensity of the α-Al and Al$_3$Ni peaks begins to decrease. As this occurs, peaks corresponding to the partially disordered Al$_9$Ni$_3$Y [88] phase appear and grow through the melting stage and into the cooling stage. A very small amount of the Al$_{26}$Ni$_6$TaY$_3$ [89] phase forms at the same time as the Al$_9$Ni$_3$Y phase (due to the small Ta impurity in these alloys (Table 1)), and maintains a constant intensity on cooling.

Rietveld analyses were performed using the methods described in Section 2.3, and examples of the fits obtained at different stages of the crystallisation process are shown in Fig. 2. A consistently high quality fit was obtained for all of the diffraction patterns prior to melting, confirming the validity of the method used to model the amorphous phase and the signal from the capillary. After melting and during the cooling stage, the relative intensities of the α-Al, Al$_3$Ni, and Al$_9$Ni$_3$Y phases became difficult to model with their respective crystal structures, as shown in Fig. 2d. This is the result of the formation of large crystals of these three phases and the corresponding reduction in particle statistics. The quality of fit therefore deteriorated during the melting and cooling stages, although the Al$_{19}$Ni$_5$Y$_3$ and Al$_{26}$Ni$_6$TaY$_3$ phases (which didn't melt completely) continued to be well modelled.

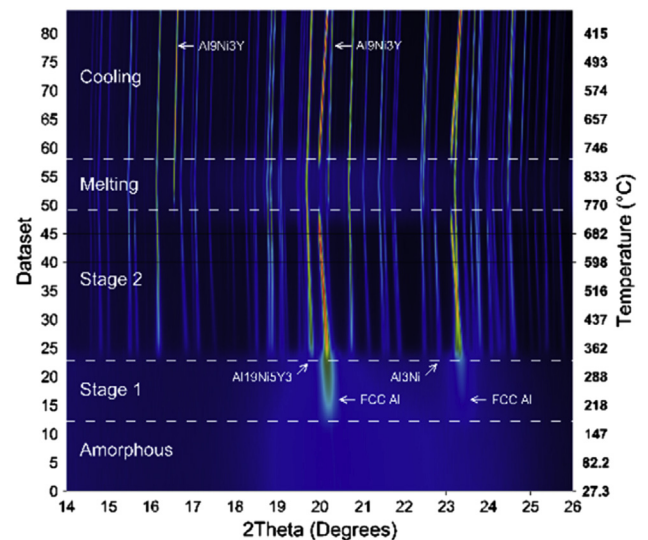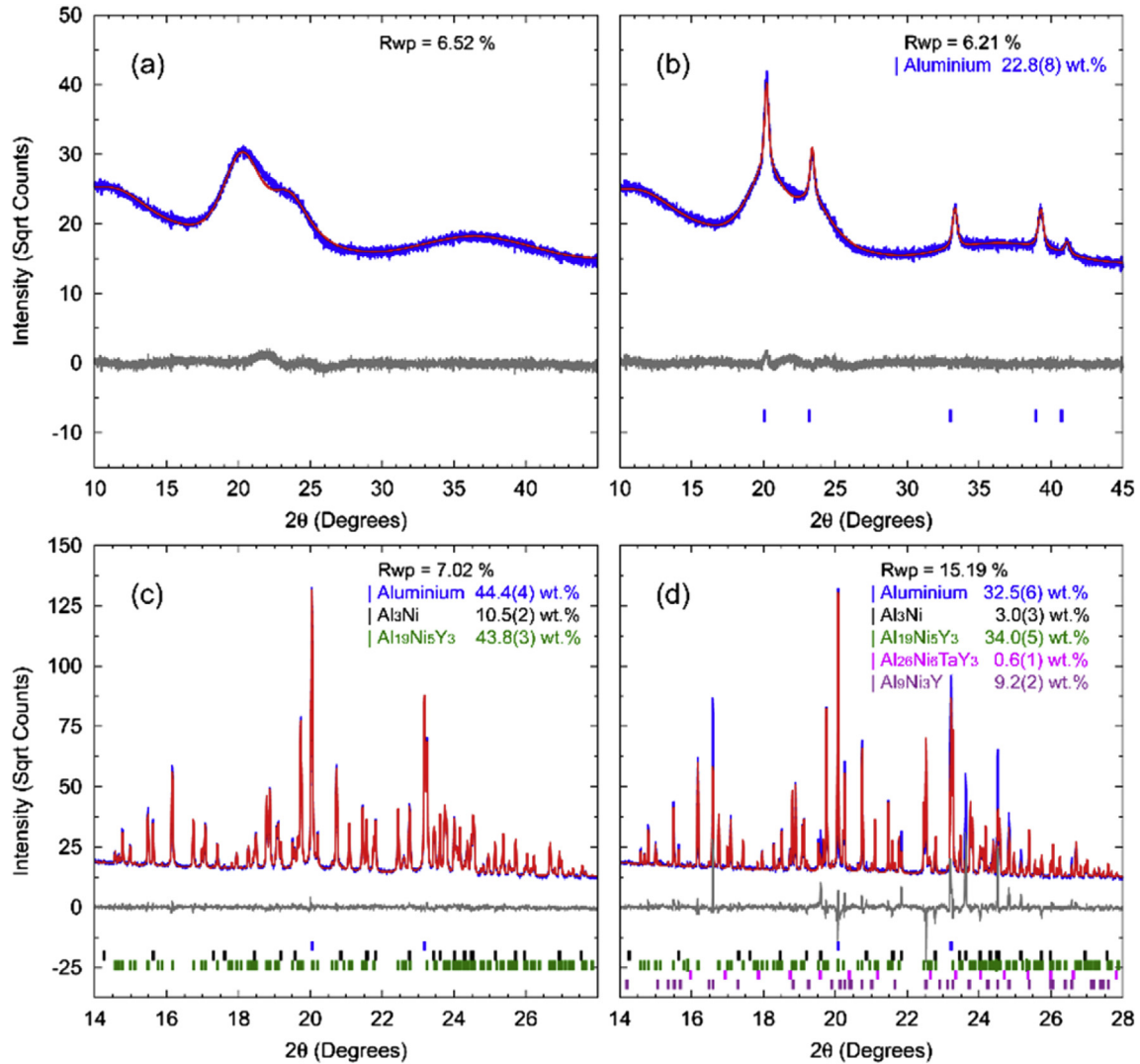**Fig. 1.** Accumulated diffraction patterns for the Al$_{87}$Ni$_9$Y$_4$ sample, viewed down the intensity axis. The different stages of the crystallisation process are indicated, and the most intense peaks for the major crystalline phases are highlighted with arrows.

Fig. 2. Observed (blue) and calculated (red) diffraction patterns from the $Al_{87}Ni_9Y_4$ sample after a) 0 min (27 °C), b) 20.9 min (218 °C), c) 55.7 min (598 °C) and d) 97.4 min (574 °C, cooling). Difference patterns are shown in grey. Excellent quality fits are obtained up until the sample begins to melt (parts a, b and c), after which large grains are formed, causing a significant reduction in particle statistics and fit quality (part d). (For interpretation of the references to colour in this figure legend, the reader is referred to the web version of this article.)

The local instrument constant K_j (Section 2.3) was calculated for each diffraction pattern in the sequence and is plotted in Fig. 3. K_j is equal to 0 prior to the formation of the first crystalline phase, as the scale factors for each phase are 0. During the first stage of crystallisation, K_j increases as the α-Al peaks grow in intensity. When the Al_3Ni and $Al_{19}Ni_5Y_3$ phases form in the second stage, K_j increases sharply, and plateaus to a constant value between 45 and 60 min into the heating cycle, indicating that the sample has reached a constant state of crystallinity. As the sample melts, K_j decreases sharply, and then rises again as the sample recrystallises during cooling, but does not reach the same high value observed prior to melting. As a point of comparison, the arbitrary scale factor applied to the peaks corresponding to the amorphous phase (I_{Glass})is also plotted in Fig. 3, and shows a strong inverse correlation with K_j, reaching a minimum value (prior to melting) at ~45 min. This result supports the validity of the proposed method for calculating the absolute phase fractions.

Assuming that the sample is completely crystalline after ~45 min (temperature ~484 °C) the maximum value of K_j was selected and employed in Equation (6) to calculate the corrected phase fractions for each diffraction pattern in the data set. The results of this quantitative phase analysis are shown in Fig. 4. The concentration of the α-Al phase increases gradually during the first stage of crystallisation, reaching a maximum of ~44 wt%. The abundance of the Al_3Ni and $Al_{19}Ni_5Y_3$ phases increase very quickly over the first 90 s of the second stage of crystallisation and ultimately reach maximum concentrations of 11 and 45 wt%, respectively, prior to melting at ~700 °C. The $Al_{19}Ni_5Y_3$ phase persists up to the highest temperature reached in this investigation of 838 °C, although a proportion of this phase is replaced by the Al_9Ni_3Y phase during the melting stage. As the sample is cooled, the α-Al and Al_3Ni phases recrystallise from the liquid. However, accurate phase quantification is hindered during the cooling stage by the irregular relative peak intensities for the α-Al, Al_3Ni and Al_9Ni_3Y phases, due to the large grains and poor particle statistics. The relative peak intensities for the $Al_{19}Ni_5Y_3$ and $Al_{26}Ni_6TaY_3$ phases are well modelled during cooling, and the calculated abundance for these two phases remains accurate.

In order to test the validity of the method used to quantify the phase fractions, the overall composition of the sample was
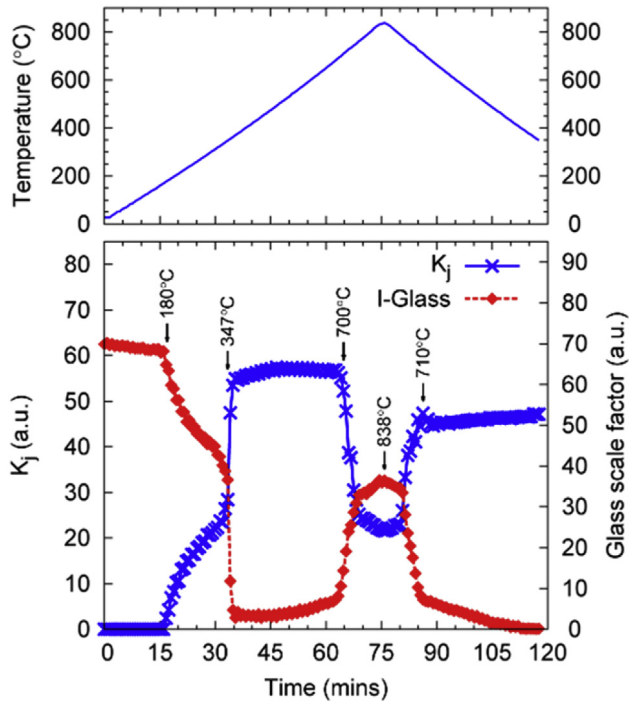
Fig. 3. Plot of the value calculated for K_j for the $Al_{87}Ni_9Y_4$ sample as a function of the time-temperature profile indicated. Note the plateau between 45 and 60 min, indicating that the sample has reached a constant state of crystallinity. Also plotted is the scale factor applied to the amorphous phase peaks (I_{Glass}), which displays an inverse correlation with K_j.

calculated at the point where the sample was estimated to be most crystalline. The composition of the sample was calculated to be $Al_{86.8}Ni_{9.1}Y_{4.1}$, which is in excellent agreement with the measured composition of the alloy (Table 1), lending further support to the proposed quantification method. This result suggests that the compositions of the α-Al, $Al_{19}Ni_5Y_3$ and Al_3Ni phases (co-existing after 45 min) are close to their stoichiometric compositions. To

further confirm the compositions of the growing phases, their compositions have been directly measured using energy dispersive spectroscopy (EDS) in TEM. A bright field TEM image of the $Al_{87}Ni_9Y_4$ alloy heated at 10 °C/min to 340 °C and then cooled is shown in Fig. 5a. The different phases are more clearly resolved in the HAADF STEM image shown in Fig. 5b. In this image, the contrast is approximately proportional to the average atomic number and we can see that the crystals are of the order of 30–50 nm in size (15–25 nm radii). The three phases present are labelled and have been identified based on their compositions. EDS point analysis indicates that the average composition of the α-Al includes 1.3 ± 0.26 Ni (at%) and 0.29 ± 0.22 Y (at%). This indicates that there is very little solute trapping occurring in the α-Al. The composition of the $Al_{19}Ni_5Y_3$ phase was measured to be 18.0 ± 1.8 Ni and 11.3 ± 1.8 Y (at%) − this composition is centered exactly on the stoichiometric composition. The composition of the Al_3Ni phase was measured to be 27.6 ± 2.8 Ni and 1.1 ± 0.6 Y (at%) − again very close to stoichiometry with a small fraction of Y solute trapping. The TEM observations further support the conclusions of the mass balance from XRD that the compositions inherited by the growing phases are close to their nominal values (i.e. solute trapping in minimal). EDS maps for Ni (Fig. 5c) and Y (Fig. 5d) illustrates the spatial distribution of the phases and the size range of 30–50 nm.

3.2. $Al_{86}Ni_{10}Y_4$ heated at 10 °C/min

Qualitatively, the $Al_{86}Ni_{10}Y_4$ sample crystallises in a similar fashion to $Al_{87}Ni_9Y_4$, via a two-stage process. This sample initially contains a small amount (~2 wt%) of the $Al_{26}Ni_6TaY_3$ phase in the as-spun state, while the remainder of the sample is amorphous. Compared to $Al_{87}Ni_9Y_4$, the α-Al phase crystallises later in the heating cycle, at ~218 °C and the formation of $Al_{19}Ni_5Y_3$ and Al_3Ni in Stage 2 occurs at about the same temperature of 347 °C.

The quantitative phase analysis for the $Al_{86}Ni_{10}Y_4$ sample is shown in Fig. 6. The concentrations of α-Al and Al_3Ni peak at 39 and 15 wt%, respectively, during Stage 2. The maximum concentration of the $Al_{19}Ni_5Y_3$ phase of ~45 wt% is equivalent to the $Al_{87}Ni_9Y_4$ sample, which may be expected given that the amount of Y is nominally the same in both samples. Compared to $Al_{87}Ni_9Y_4$, more
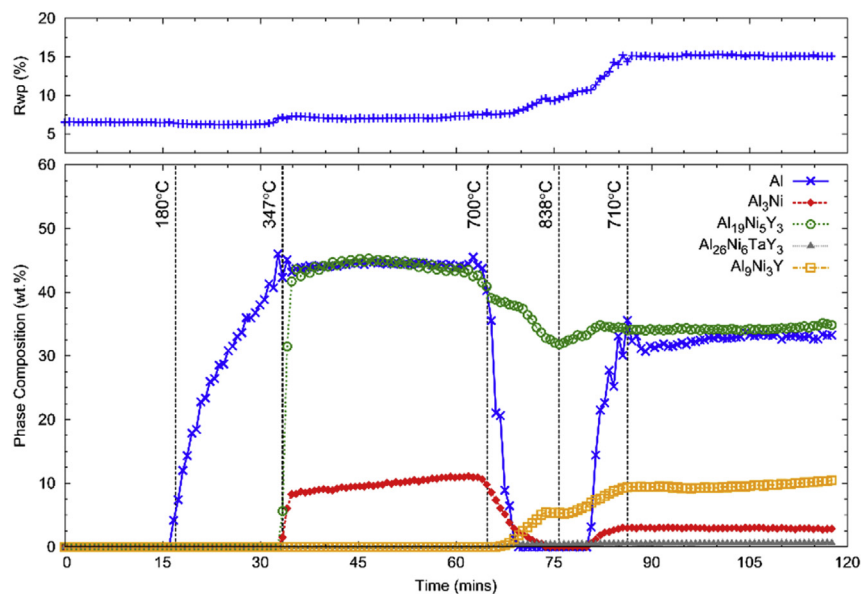
Fig. 4. Analysed phase composition (wt%) as a function of time, along with the weighted profile R factor (R_{wp}) for the $Al_{87}Ni_9Y_4$ sample. Note that as the sample melts at 710 °C, the R_{wp} begins to increase until the sample re-solidifies, after which it remains fairly constant. The poor particle statistics observed after melting means that some crystalline material is unaccounted for during this period.
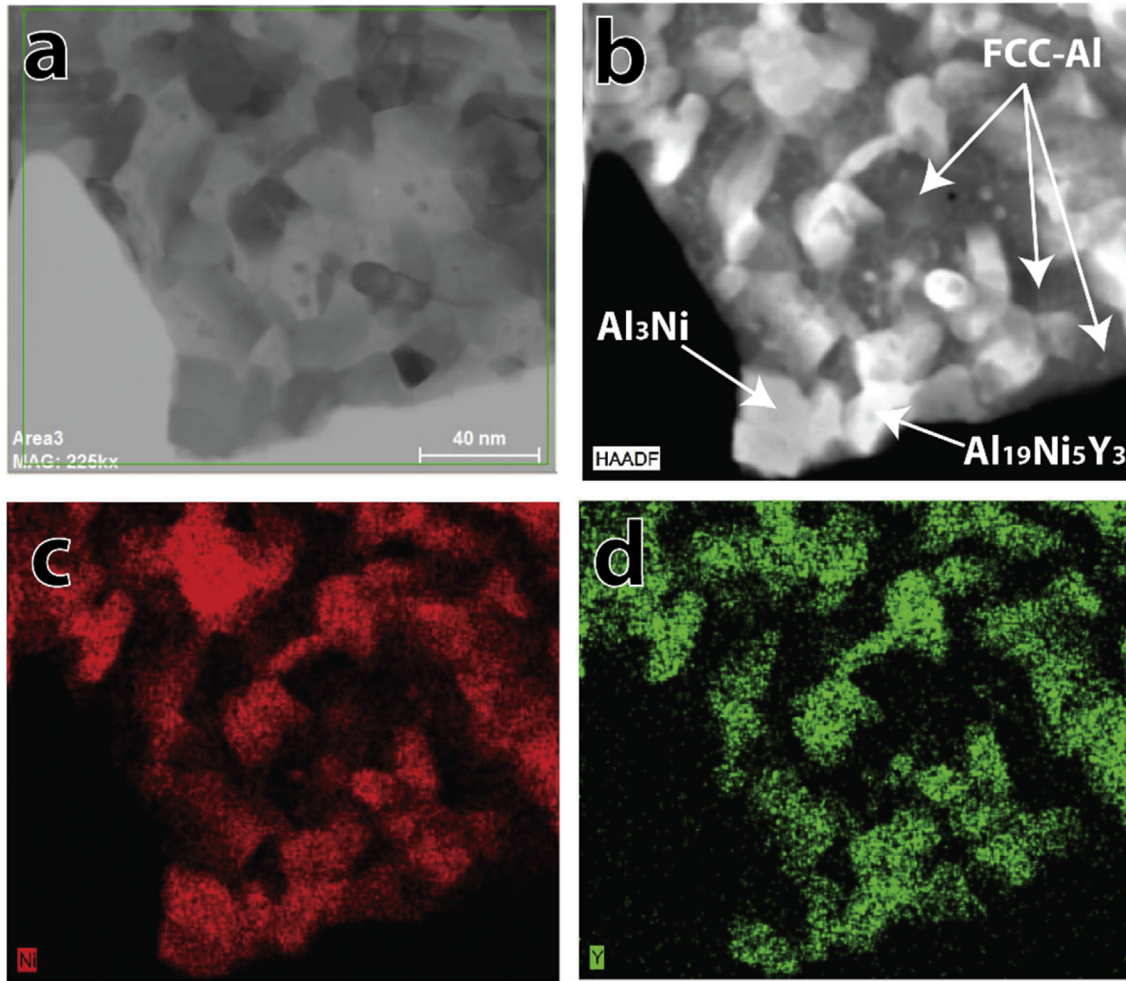
Fig. 5. Sample of the $Al_{87}Ni_9Y_4$ alloy heated to 340 °C at a rate of 10 °C/min then cooled to room temperature. The microstructure consists of α-Al, $Al_{19}Ni_5Y_3$ and a small amount of Al_3Ni. a) Bright field TEM image, b) High angle annular dark field (HAADF) STEM image, c) EDS Ni map of the same region shown in a) and b), d) EDS map of Y.
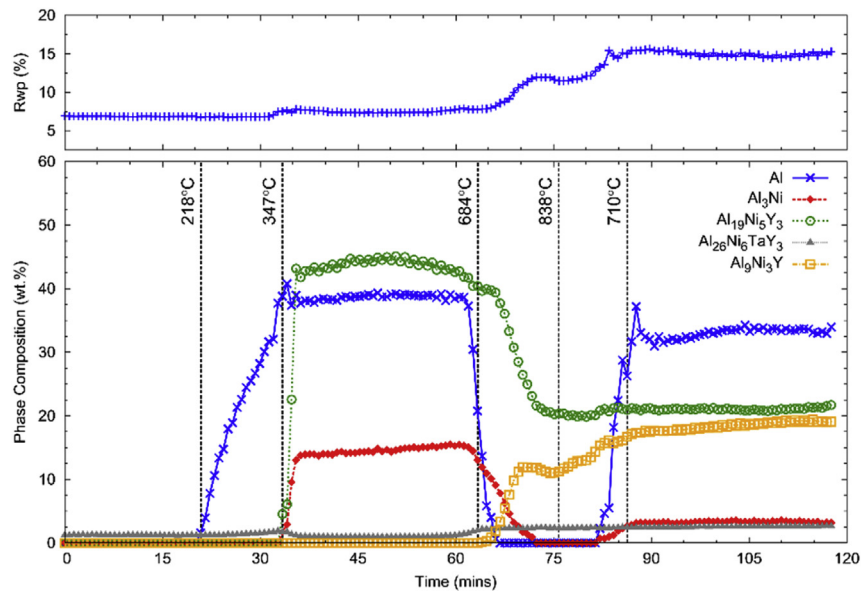
Fig. 6. Analysed phase composition (wt%) as a function of time, along with the weighted profile R factor (R_{wp}) for the $Al_{86}Ni_{10}Y_4$ sample.

of the $Al_{19}Ni_5Y_3$ and Al_3Ni phases are consumed during the melting stage to form the Al_9Ni_3Y phase, which continues to increase in concentration during cooling. There is also a gradual increase in the $Al_{26}Ni_6TaY_3$ phase after melting, and a similar amount of α-Al is formed upon cooling. The overall composition of this sample was calculated (at the point of maximum crystallinity) to be $Al_{85.3}Ni_{10.5}Y_{4.2}$ (with ~0.02 at% Ta) which is in excellent agreement with the composition measured by ICP for this sample (Table 1) and again indicates that the phases present at maximum crystallinity adopt compositions close to their stoichiometric compositions.

3.3. $Al_{83}Ni_{13}Y_4$ heated at 10 °C/min

Unlike $Al_{87}Ni_9Y_4$ and $Al_{86}Ni_{10}Y_4$, the $Al_{83}Ni_{13}Y_4$ alloy crystallises in three stages (Fig. 7). The sample is initially completely amorphous, however the first crystalline phase to form is the metastable Al_9Ni_2 phase [90,91] (based on the monoclinic Al_9Co_2 structure [92]) at a temperature of ~274 °C. As the temperature increases, α-Al gradually forms with the Al_9Ni_2 phase. Once the temperature reaches ~360 °C, the Al_9Ni_2 phase starts to decompose, forming Al_3Ni and beginning the second stage of crystallisation. It is not until ~395 °C, once the Al_9Ni_2 phase is no longer visible, that the $Al_{19}Ni_5Y_3$ phase begins to form, signalling the third stage of crystallisation. Compared to the previous samples, the melting stage begins at a lower temperature of 665 °C.

Examples of the Rietveld fits obtained at different crystallisation stages of the $Al_{83}Ni_{13}Y_4$ sample are shown in Fig. 8. The amorphous phase is well modelled, however, during the first stage of crystallisation there are some significant discrepancies between the observed and calculated peaks for the Al_9Ni_2 phase (Fig. 8b), suggesting that the crystal structure model in the literature may not be an ideal description of the phase formed in this setting. As the Al_9Ni_2 phase decomposes in the second crystallisation stage, the intensity of the Al_3Ni peaks increase, and quickly becomes the dominant phase in the diffraction patterns, as highlighted in Fig. 8c. During this stage, a small number of broad peaks briefly appear in the diffraction patterns, which may indicate an unidentified phase. However, the low intensity of these peaks suggests that it is present at a very low concentration. Once the $Al_{19}Ni_5Y_3$ phase forms in the third crystallisation stage, the quality of fit improves (Fig. 8d) and
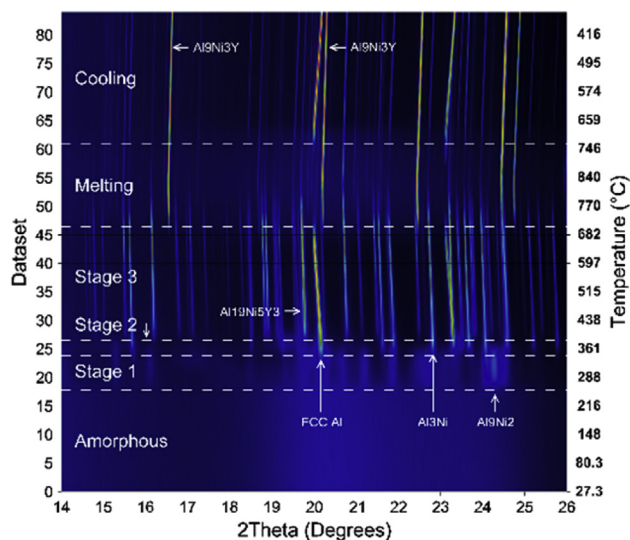

Fig. 7. Accumulated diffraction patterns for the $Al_{83}Ni_{13}Y_4$ sample, viewed down the intensity axis. Note that there are three stages in the crystallisation process for this sample.

the maximum value for K_j is obtained ~55 min into the heating cycle, indicating that the sample is most crystalline at this point.

The quantitative phase analysis shown in Fig. 9 reveals that the concentration of the Al_9Ni_2 phase peaks at over 60 wt% during the first stage of crystallisation. Combined with the ~25 wt% of α-Al phase present at this time, over 85 wt% of the sample is crystalline. As the Al_9Ni_2 phase decomposes, a transient excess of the Al_3Ni phase forms, peaking at a maximum concentration of 48 wt%. Only after the Al_9Ni_2 phase has completely decomposed does the $Al_{19}Ni_5Y_3$ phase begin to form, reaching a maximum concentration of ~43 wt% similar to the previous alloys, whilst the Al_3Ni concentration decreases to a steady value of 28 wt%. During the melting stage, the $Al_{19}Ni_5Y_3$ phase is almost completely consumed to form the partially disordered Al_9Ni_3Y phase. Based on the quantitative phase analysis, the composition of this sample was calculated to be $Al_{82.8}Ni_{13.2}Y_{3.9}$ at the point of maximum crystallinity, which is again in very good agreement with the measured composition of this alloy (Table 1).

3.4. $Al_{81}Ni_{15}Y_4$ heated at 10 °C/min

The $Al_{81}Ni_{15}Y_4$ sample also crystallises via a three-stage process. The metastable Al_9Ni_2 phase is the first to form at a temperature of ~287 °C. In this composition, the Al_3Ni also forms during the first stage of crystallisation, alongside Al_9Ni_2 and α-Al. The Al_9Ni_2 phase decomposes at a slightly lower temperature, ~350 °C, and the second stage of crystallisation extends over a significantly wider range of temperatures than in the $Al_{83}Ni_{13}Y_4$ alloy. The same set of broad, unidentified peaks is observed during this stage with a slightly stronger intensity than in $Al_{83}Ni_{13}Y_4$. At 414 °C the $Al_{19}Ni_5Y_3$ phase begins to form signalling the third stage of crystallisation. Melting also occurs over a wider range of temperatures compared to previous samples, beginning at ~640 °C. During the melting stage the $Al_{19}Ni_5Y_3$ phase appears to be completely replaced by the Al_9Ni_3Y phase and does not reappear on cooling.

The results of the quantitative phase analysis for the $Al_{81}Ni_{15}Y_4$ sample are shown in Fig. 10. Compared to the $Al_{83}Ni_{13}Y_4$ sample, significantly less of the metastable Al_9Ni_2 phase is produced in the first stage of crystallisation, while considerably more Al_3Ni forms during the second stage, reaching a maximum concentration of ~65 wt%. The apparent oscillations in the α-Al phase fractions during the first stage is an artefact from a period of strong overlap with the peaks of the Al_9Ni_2 and Al_3Ni phases, combined with the fact that one of the detector gaps was located over the (111) peak of α-Al in alternating data sets in this temperature range. In the third crystallisation stage, the $Al_{19}Ni_5Y_3$ phase reaches a maximum concentration of ~41 wt% prior to being completely replaced by the Al_9Ni_3Y phase during melting. At the end of the cooling stage, the concentration of the Al_9Ni_3Y phase reaches a maximum of ~39 wt%, which is the highest concentration observed in any of the samples. A small amount (<1 wt%) of the $Al_{26}Ni_6TaY_3$ phase forms at the same time as Al_9Ni_3Y, and remains constant during cooling. The maximum crystallinity is observed towards the end of the third stage of crystallisation, about 50 min into heating cycle, at which point the composition of the alloy is calculated to be $Al_{80.8}Ni_{15.3}Y_{3.9}$ which again compares very well with the measured composition of the alloy (Table 1).

3.5. $Al_{75}Ni_{15}Y_{10}$ heated at 10 °C/min

In order to investigate the role of Y in the crystallisation of Al-Ni-Y alloys, a sample with a composition of $Al_{75}Ni_{15}Y_{10}$ was also studied. In this composition, $Al_{19}Ni_5Y_3$ is the principal phase to form in the one and only crystallisation stage of the glassy matrix, which begins at a temperature of ~375 °C. α-Al also forms gradually
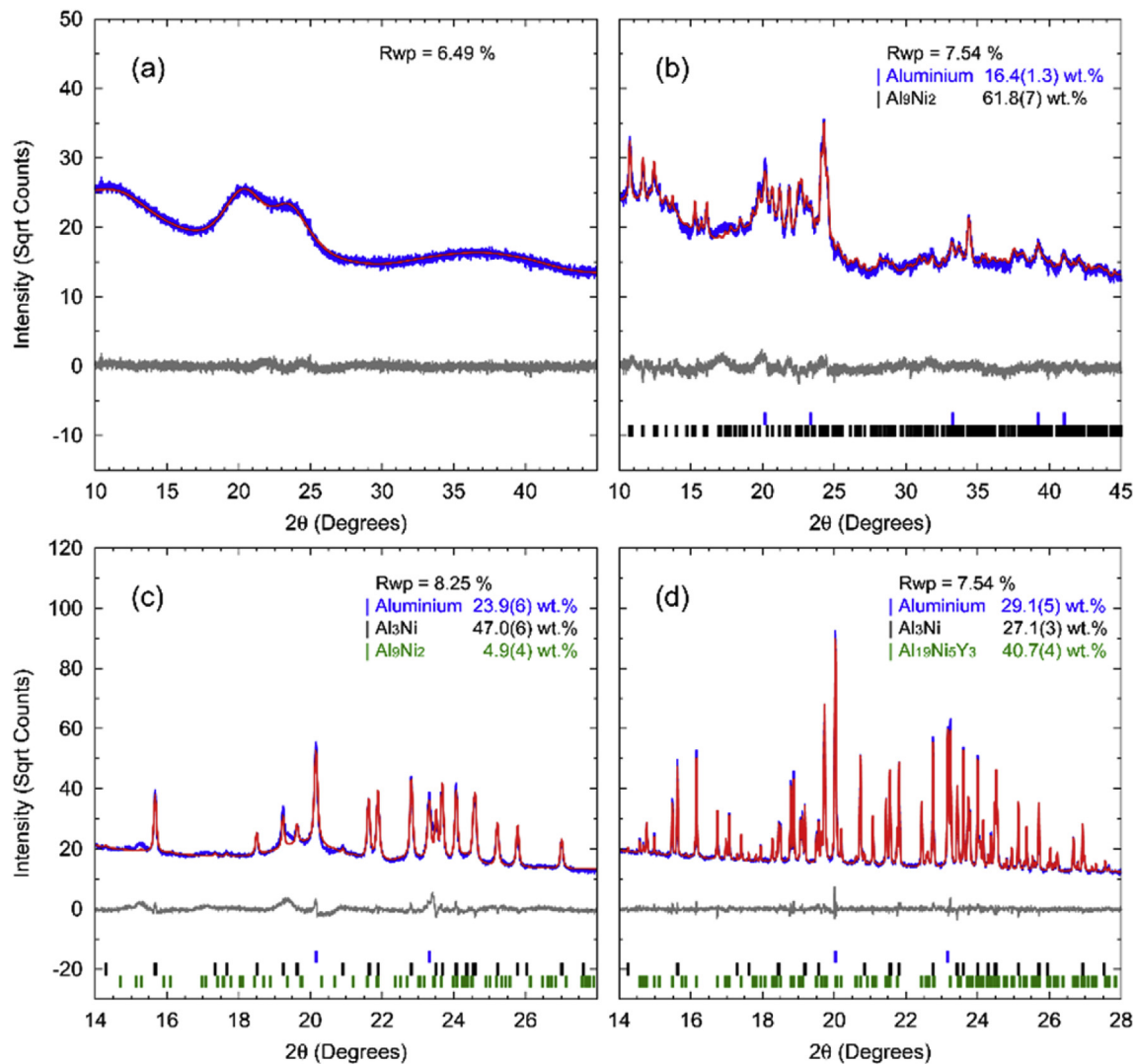
Fig. 8. Observed (blue) and calculated (red) diffraction patterns from the $Al_{83}Ni_{13}Y_4$ sample after a) 0 min (27 °C), b) 30.6 min (317 °C), c) 36.2 min (376 °C) and d) 55.7 min (597 °C). Difference patterns are shown in grey. The model for the Al_9Ni_2 phase fits the observed data reasonably well (part b), however there are some discrepancies that may indicate that the structure is not completely correct. (For interpretation of the references to colour in this figure legend, the reader is referred to the web version of this article.)

during this stage, and weak peaks from the Al_3Y phase appear as the temperature is increased instead of the Al_3Ni seen in the previous alloys. At ~560 °C, peaks corresponding to the $Al_{23}Ni_6Y_4$ phase [93] appear, apparently at the expense of the $Al_{19}Ni_5Y_3$ phase, and increase in intensity up to the maximum temperature of ~830 °C encountered in this experiment. This is the only alloy where the $Al_{23}Ni_6Y_4$ phase is observed. The α-Al and Al_3Y phases melt at ~625 °C, and reappear at a similar temperature during cooling. Unlike the previous alloy compositions, high quality fits were also obtained during the cooling stage for this alloy, and the highest level of crystallinity is observed at the very end of the thermal treatment, after the sample has re-solidified.

The results of the quantitative phase analysis for the $Al_{75}Ni_{15}Y_{10}$ sample are shown in Fig. 11. During the first stage of crystallisation, the concentration of the $Al_{19}Ni_5Y_3$ phase quickly increases to ~80 wt%. As the temperature increases into the melting stage, the concentration of the $Al_{19}Ni_5Y_3$ phase reduces to a minimum ~36 wt %, while the $Al_{23}Ni_6Y_4$ phase peaks at a maximum concentration of ~37 wt% at the same time, indicating that a large proportion of the $Al_{19}Ni_5Y_3$ phase is replaced by $Al_{23}Ni_6Y_4$. Upon cooling, the $Al_{23}Ni_6Y_4$ phase begins to revert back to $Al_{19}Ni_5Y_3$ until the α-Al

and Al_3Y phases recrystallise from the melt, after which the transformation slows down significantly. The higher stability of the $Al_{19}Ni_5Y_3$ phase relative to the $Al_{23}Ni_6Y_4$ phase is an interesting observation, as the $Al_{19}Ni_5Y_3$ phase has previously been thought to be metastable [52,94]. During the cooling stage, K_j continues to increase slowly, not quite reaching a steady value before the final dataset, suggesting that some amorphous material may still be present at the end of the heating cycle. However, using the maximum value for K_j observed in the final dataset, the composition of the alloy is calculated to be $Al_{75.0}Ni_{15.3}Y_{9.7}$, which is in very good agreement with the composition measured by ICP (Table 1). Therefore, the fraction of any remaining amorphous phase is likely to be small.

3.6. Crystallite size and number density

The width of the peaks in a diffraction pattern can provide an insight into the average crystallite size of the different phases. When combined with knowledge of the volume fractions derived from the quantitative phase analysis, estimates of the number density can also be obtained for the crystalline phases. The average
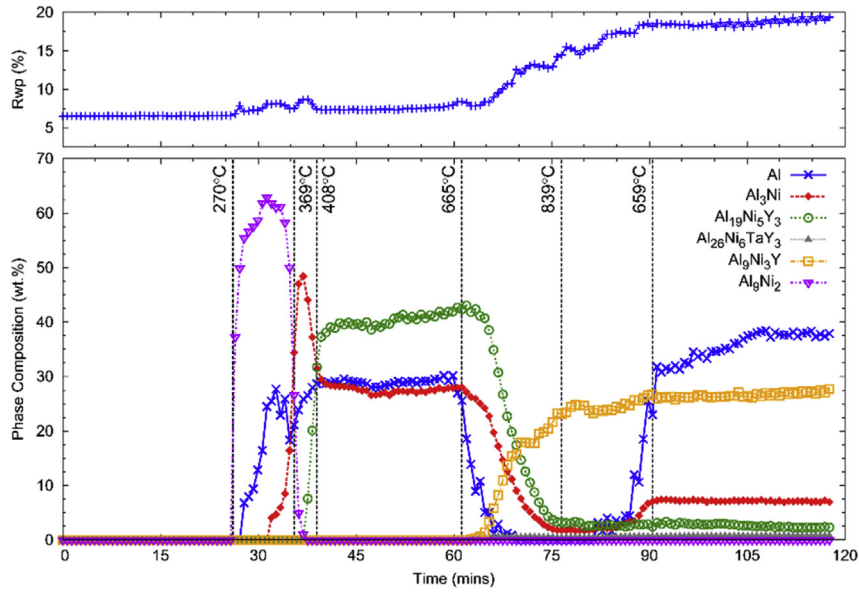
Fig. 9. Analysed phase composition (wt%) as a function of time, along with the weighted profile R factor (R_{wp}) for the $Al_{83}Ni_{13}Y_4$ sample. Note the formation of the Al_9Ni_2 phase in the first stage of the crystallisation process, followed by the transient formation of excess Al_3Ni.
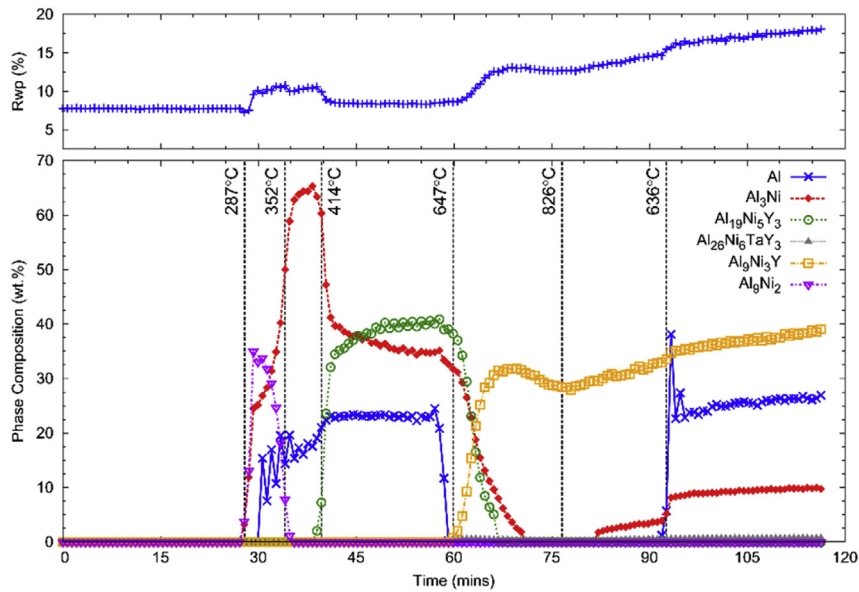
Fig. 10. Analysed phase composition (wt%) as a function of time, along with the weighted profile R factor (R_{wp}) for the $Al_{81}Ni_{15}Y_4$ sample. Note the transient formation of a substantial amount of Al_3Ni in the second stage of crystallisation.

crystallite sizes were calculated using the volume-weighted integral breadth method [95] for the phases formed in the early stages of crystallisation, and the crystallite radii are summarised in Fig. 12a–d. In the $Al_{87}Ni_9Y_4$ and $Al_{86}Ni_{10}Y_4$ samples, the radii of the α-Al crystallites are initially around 5–10 nm, and evolve slowly over the first stage of crystallisation. Once the intermetallic phases form in the second stage, the radii of the α-Al crystallites increase rapidly to ~24 nm, and proceed to increase quickly thereafter. To provide some 'direct space' measurements of phase radii to compare with those obtained from the Rietveld refinement we can consider the TEM image shown in Fig. 5 for the $Al_{87}Ni_9Y_4$ alloy heated to just above 340 °C; under this condition the microstructure is dominated by α-Al and $Al_{19}Ni_5Y_3$ together with a small amount of Al_3Ni (Fig. 4). In this TEM image the phases are

~30–50 nm in size (radii of ~15–25 nm) which compares very well with the XRD radii indicated in Fig. 12a after 30–35 min of ~10–25 nm. This comparison should provide confidence in the radii extracted from the Rietveld refinement of the high resolution XRD data.

In the $Al_{83}Ni_{13}Y_4$ and $Al_{81}Ni_{15}Y_4$ samples, the Rietveld refinement of the Al_9Ni_2 crystallite size was found to be unstable because of the peak overlap highlighted in Fig. 8b. The value of this parameter was refined using the dataset containing the maximum concentration of this phase, giving an average crystallite radius of ~5.3 nm. Assuming that the crystallite size of Al_9Ni_2 does not change significantly during the first stage of crystallisation (similar to the behaviour observed for α-Al in the previous samples), the value was fixed for all other refinements. The rapid increase in the
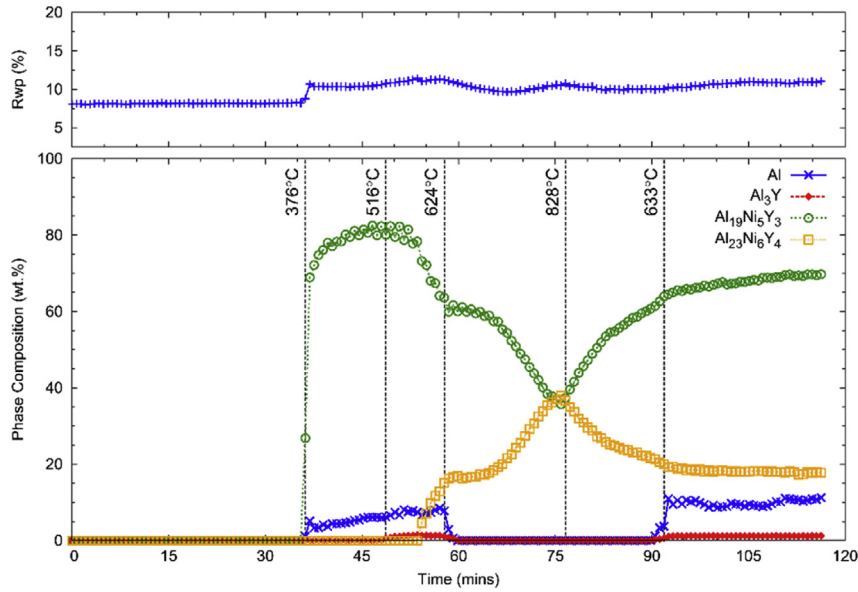
Fig. 11. Analysed phase composition (wt%) as a function of time, along with the weighted profile R factor (R_{wp}) for the $Al_{75}Ni_{15}Y_{10}$ sample. Note the reversible transformation between the $Al_{19}Ni_5Y_3$ and $Al_{23}Ni_6Y_4$ phase with temperature.
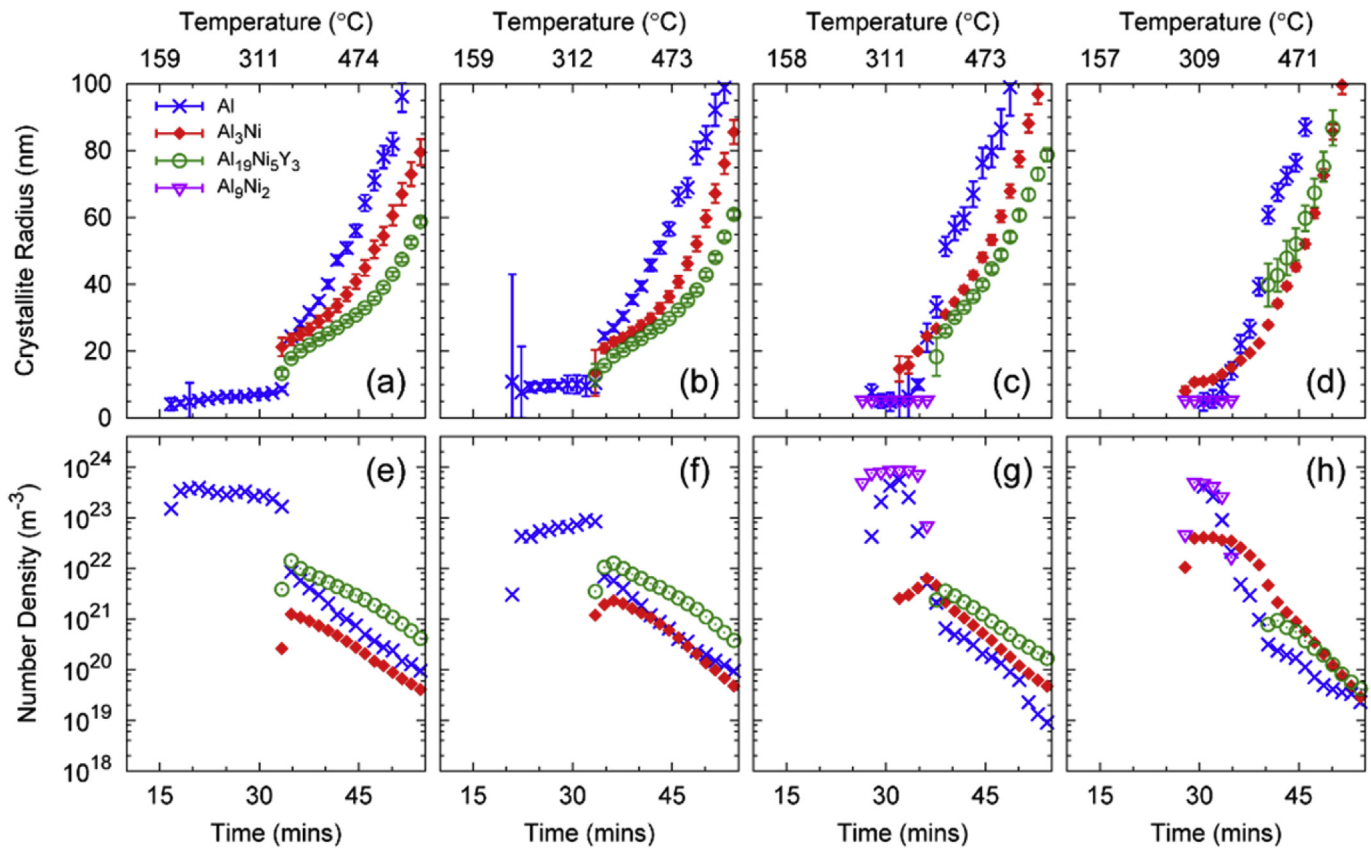

Fig. 12. Evolution of the average crystallite radii for the crystalline phases observed in the a) $Al_{87}Ni_9Y_4$, b) $Al_{867}Ni_{10}Y_4$, c) $Al_{83}Ni_{13}Y_4$, and d) $Al_{81}Ni_{15}Y_4$, alloys. The estimated number densities for the crystallites in the same alloys are shown in e) to h), respectively.

crystallite size of the α-Al phase was less pronounced in $Al_{83}Ni_{13}Y_4$ and $Al_{81}Ni_{15}Y_4$ samples, whilst the crystallite sizes of the Al_3Ni and $Al_{19}Ni_5Y_3$ phases increased more rapidly. The evolution of the crystallite sizes of the α-Al and $Al_{19}Ni_5Y_3$ phases in the $Al_{75}Ni_{15}Y_{10}$ sample was found to be similar to the $Al_{83}Ni_{13}Y_4$ and $Al_{81}Ni_{15}Y_4$
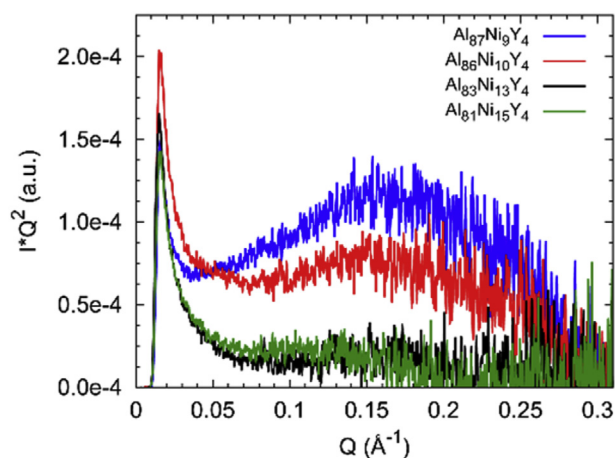
samples (Fig. 12c–d).

In order to estimate the number densities for each phase it is necessary to convert the weight fractions from the quantitative phase analysis into volume fractions. To do this the crystallographic densities were used for each phase, with the exception of the glassy

phase, which was assumed to be a constant 2.7 g/cm^3. Different values for the glass density (up to 4.0 g/cm^3) were trialled, and found to have only a small effect on the calculated number densities compared to changes in the crystallite size. The results of the number density calculations are shown in Fig. 12e−h. In the $Al_{87}Ni_9Y_4$ and $Al_{86}Ni_{10}Y_4$ samples, the estimated number densities for the α-Al phase peak at ~4 × 10^{23} m^{-3} and ~9 × 10^{22} m^{-3}, respectively, during the first stage of crystallisation. However, α-Al is not the only crystalline phase to form with such high number densities. In the $Al_{83}Ni_{13}Y_4$ and $Al_{81}Ni_{15}Y_4$ samples, the high volume fraction and small crystallite size of the Al_9Ni_2 phase result in even higher number densities of ~9 × 10^{23} m^{-3} and ~5 × 10^{23} m^{-3}, respectively.

3.7. SAXS investigation of the as-spun ribbons

One of the proposed explanations for the high number densities of FCC α-Al observed during crystallisation of Al glasses is the existence of Al-rich nanoscale heterogeneities. To investigate the existence of such chemical heterogeneities, which may include crystalline nuclei below the detection limit of powder diffraction [59,65−67], SAXS measurements were performed on the as-spun ribbons. The results of this analysis are shown in Fig. 13, using the Kratky representation [96]. Peaks in Kratky plots indicate the presence of objects with different electron densities to the surrounding material. The position and width of the peaks are related to the size and size distribution of these objects. It can be seen from Fig. 13 that the $Al_{87}Ni_9Y_4$ sample contains a broad hump centred at ~0.16 Å^{-1}, indicating a significant number of objects with an average radius of ~1.08 nm. The $Al_{86}Ni_{10}Y_4$ sample also contains a smaller hump at ~0.15 Å^{-1}, indicating the presence of slightly larger objects (~1.15 nm radius) but at a lower apparent concentration. The existence of such heterogeneities is consistent with a hypothesis involving catalysed α-Al nucleation by Al-rich heterogeneities, although further work with complementary techniques is required to confirm the identity of the heterogeneities. However, the Al_9Ni_2 phase forms with an even higher number density in the $Al_{83}Ni_{13}Y_4$ and $Al_{81}Ni_{15}Y_4$ alloys and these samples do not have distinct peaks in the Kratky plots, suggesting that the matrix material is quite homogenous over the size range investigated here. It is possible that there are heterogeneities at larger length scales, such as phase separated regions on the order of 10−100 nm [59,61−64], which
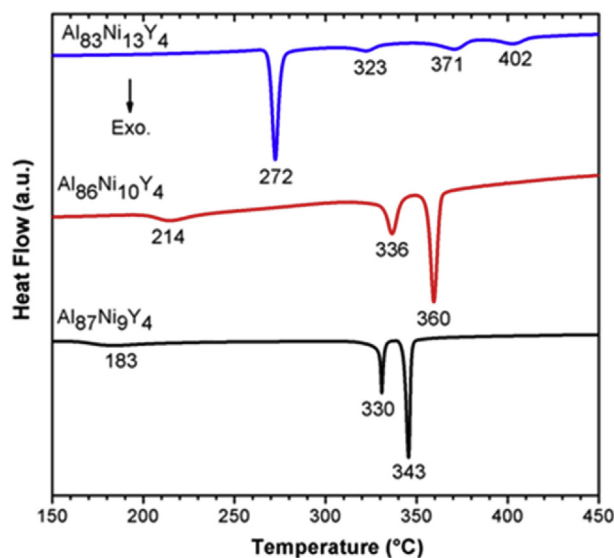
would require further investigation.

4. Discussion

4.1. Crystallisation temperatures

The crystallisation temperatures of metallic glasses are usually determined using differential scanning calorimetry (DSC), and Jindal [97] has recently applied DSC to the same $Al_{87}Ni_9Y_4$, $Al_{83}Ni_{10}Y_4$, and $Al_{83}Ni_{13}Y_4$ alloys examined here. The results of these DSC measurements are reproduced in Fig. 14. Whilst it was known previously that the first crystallisation event in the $Al_{87}Ni_9Y_4$ and $Al_{83}Ni_{10}Y_4$ alloys was the formation of α-Al, the identity and order of formation of other crystalline phases was not known. From the results of the quantitative phase analysis presented in Section 3, it is now understood that the second and third crystallisation events in the $Al_{87}Ni_9Y_4$ and $Al_{83}Ni_{10}Y_4$ alloys correspond to the formation of the Al_3Ni and $Al_{19}Ni_5Y_3$ phases, respectively. Although the Al_3Ni and $Al_{19}Ni_5Y_3$ phases appear to form simultaneously in the diffraction data, it should be noted that each diffraction pattern represents the average state of the sample over a ~5 °C window, and the identification is therefore based on the relative fractions of Al_3Ni and $Al_{19}Ni_5Y_3$. For the $Al_{83}Ni_{13}Y_4$ sample, the first crystallisation event can now be associated with the formation of the metastable Al_9Ni_2 phase. The second, third and fourth crystallisation events are related to the formation of α-Al, Al_3Ni and $Al_{19}Ni_5Y_3$ phases, respectively. Table 2 compares the crystallisation temperatures observed during the *in situ* powder diffraction experiment, and those reported by Jindal [97] using DSC with the same heating rate as used in the *in situ* powder diffraction experiments reported here. Considering the precision of the temperature calibration (±7.5 °C), and the averaging involved in the diffraction data, the agreement between the crystallisation temperatures is excellent.

4.2. Structural features of the glassy matrix

The amorphous features in XRD patterns collected from metallic glasses are often discussed in terms of either phase separation [61−64] or quenched-in nuclei [59,65−67], and the distinction

Fig. 13. Radially averaged SAXS data in the Kratky representation, collected from the $Al_{87}Ni_9Y_4$, $Al_{86}Ni_{10}Y_4$, $Al_{83}Ni_{13}Y_4$, and $Al_{81}Ni_{15}Y_4$ samples in the as-spun condition. Note the humps at ~0.16 Å^{-1} and ~0.15 Å^{-1} in a) and b), respectively, indicating the presence of nanometre scale objects.

Fig. 14. DSC curves of as-spun $Al_{87}Ni_9Y_4$, $Al_{86}Ni_{10}Y_4$ and $Al_{83}Ni_{13}Y_4$ metallic glasses reported by Jindal [97], showing the temperatures at which the different crystallisation events occur at a heating rate of 10 °C/min.

Table 2
Comparison between the crystallisation temperatures observed during the *in situ* powder diffraction experiment, and DSC results reported by Jindal [97]. XRD temperatures have been taken from the first appearance of the phase.

Sample	Phase	XRD temp (°C)	DSC temp (°C)
$Al_{87}Ni_9Y_4$	α-Al	180	183
	Al_3Ni	347	330
	$Al_{19}Ni_5Y_3$	347	343
$Al_{86}Ni_{10}Y_4$	α-Al	218	214
	Al_3Ni	347	336
	$Al_{19}Ni_5Y_3$	347	360
$Al_{83}Ni_{13}Y_4$	Al_9Ni_2	274	272
	α-Al	297	323
	Al_3Ni	347	371
	$Al_{19}Ni_5Y_3$	399	402

between these can have a significant bearing on the competition in phase formation during crystallisation. In the Al-Ni-Y system, Sabet-Sharghi et al. [65] previously observed a systematic change in the relative intensities of the three main amorphous peaks depending on the Ni:Y ratio. A similar systematic variation is observed in the present investigation, as shown in Fig. 15.

The composition of the samples studied by Sabet-Sharghi *et al.* obeyed the formula $Al_{85}Ni_{15-x}Y_x$, and the intensity of the so-called "shoulder" peak (23–24° 2θ in Fig. 15), located to the right of the main peak (~20° 2θ), was found to increase with Ni concentration (decrease with Y). As the shoulder peak appeared to coincide with the formation of α-Al during crystallisation of their samples, this was interpreted as evidence for the existence of quenched-in α-Al nuclei below the detection limit of XRD. Similar observations have been made by others [66]. Whilst the intensity of the shoulder peak also increases with Ni concentration in the present investigation (Fig. 15), the *in situ* XRD results show that the first crystallisation product switches from α-Al to Al_9Ni_2. Furthermore, the SAXS data do not support the hypothesis that the shoulder peak corresponds

Fig. 15. Comparison of the amorphous scattering observed for the as-spun ribbons *t* minutes into the *in situ* XRD experiment. Note the "shoulder" to the right of the main peak increases in relative intensity with increasing Ni concentration. The shape and intensity of the amorphous peaks do not change significantly prior to crystallisation, as shown for the $Al_{87}Ni_9Y_4$ sample. The sharp peaks in the $Al_{86}Ni_{10}Y_4$ sample are due to a minor concentration of crystalline $Al_{26}Ni_6TaY_3$ (see Section 3.2).

to quenched-in α-Al or Al_9Ni_2 nuclei, as there is no indication of nanometre-scale objects in the high Ni concentration alloys.
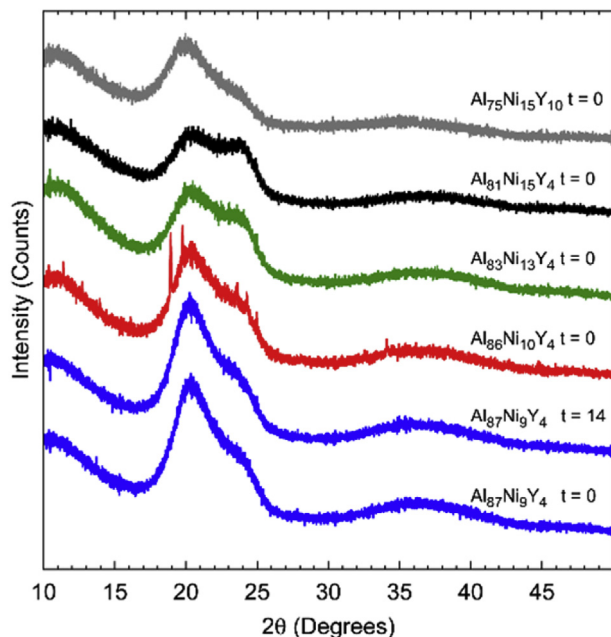
The concentration of Y was fixed at 4 at% for four of the five samples examined in our study, so it would appear that the relative intensities of the main and shoulder peaks are related to the Ni concentration. However, in the $Al_{75}Ni_{15}Y_{10}$ alloy, the increased Y concentration had the effect of reducing the shoulder peak and increasing the intensity of the main peak, relative to the $Al_{81}Ni_{15}Y_4$ alloy. Interestingly, the $Al_{19}Ni_5Y_3$ phase is the first major phase to form during the crystallisation of this alloy, with only a relatively small fraction of α-Al. This indicates that the main peak should not be interpreted as evidence for α-Al nuclei either. This conclusion is in agreement with the nuclear magnetic resonance (NMR) results of Lay et al. [67].

If neither of the amorphous peaks in the XRD patterns are due to nanometre-scale crystalline nuclei, then the most likely explanation is that they are produced by two different types of local ordering within the as-spun ribbons, and could correspond to the phase separation observed in TEM studies (e.g. Refs. [59,64]). If this is the case, then the results in Fig. 15 would suggest that, for given synthesis conditions, increasing the Ni concentration has a destabilising effect on the glass, causing an increase in the degree of phase separation, while increasing the Y concentration has a stabilising effect, reducing phase separation. Interestingly, the size and shape of the two amorphous peaks did not change significantly during the *in situ* heating experiments (e.g. $Al_{87}Ni_9Y_4$ in Fig. 15), suggesting that the phase separated regions (if present) do not evolve rapidly at temperatures below the initial crystallisation point.

4.3. Competition in phase formation during crystallisation

A number of different hypotheses have been proposed to explain the high number densities of α-Al observed after crystallisation of glassy Al alloys. As shown in Section 3.6, these high number densities are not only associated with α-Al, Ni containing intermetallic phases also form with equally high number densities. The series of alloys considered in this study traverses a range of compositions where the first phase to form varies from α-Al ($Al_{87}Ni_9Y_4$ and $Al_{86}Ni_{10}Y_4$) to Al_9Ni_2 ($Al_{83}Ni_{13}Y_4$ and $Al_{81}Ni_{15}Y_4$). The different hypotheses for the high nucleation rates will manifest themselves differently for each phase, and hence by examining the competition in phase formation some inferences can be made regarding different potential effects.

The competition in phase formation depends on the competition in both nucleation and growth, although of course a phase must first be able to nucleate before any growth advantage is considered. Emphasis here will be focused only on the first stage of crystallisation where the phases are nucleating and growing in the amorphous matrix without the complications of other phases being present (and their associated interfaces and solute profiles) such as during Stages 2 and 3 of the crystallisation process. During this first crystallisation stage the phases have sizes of 5–10 nm (Fig. 12a–d). A starting point for examining the competition in nucleation is to consider nucleation in a perfectly homogeneous matrix using classical nucleation theory (CNT). This should not be expected to give quantitative agreement, however the predicted trends in the competition in phase formation will be very informative. The XRD and TEM both suggest that the phases form with close to their equilibrium compositions and as a result precipitate growth will be controlled by long-range diffusion. A good estimate of the competition in growth may be made by considering the growth rate of spherical precipitates using Zener's classic diffusion controlled solution [98]. Since all phases must partition Ni and Y during growth in the alloys considered (Fig. 5), the rate-limiting

diffusion species is the same for all phases and the competition in growth may be found by simply comparing the thermodynamic factors of Zener's growth rate equation: for solute rich precipitates: $\frac{C_0-C_e}{C_\beta-C_e}$, and for solute poor precipitates: $\frac{C_e-C_0}{C_0-C_\beta}$ where C_0 is the bulk alloy solute content, C_β is the solute content of the growing phase and C_e is the local equilibrium solute content in the amorphous matrix at the precipitate/matrix interface.

The thermodynamic calculations required for comparisons of calculated nucleation and growth rates were performed using the thermodynamic assessment of Golumbfskie et al. [73] (modified to include the thermodynamic description of the Al_9Ni_3Y phase obtained from his PhD thesis [74]). To first check the accuracy of this thermodynamic assessment, a comparison was made between the experimentally observed phase fractions at the point of maximum crystallinity prior to melting, and the (constrained) equilibrium values calculated using the assessment of Golumbfskie et al. The results presented in Table 3 show excellent agreement, providing some confidence in the thermodynamic assessment at the temperatures probed in the XRD experiments [73,74]. To perform the constrained equilibrium calculations, the Al_3Y phase (Al_3Ni in the case of the $Al_{75}Ni_{15}Y_{10}$ sample), which is predicted to be more stable than the $Al_{19}Ni_5Y_3$ phase, was suspended since it was not observed experimentally.

Using the thermodynamic description of Golumbfskie et al. the nucleation barrier $\left(\Delta G^* = 16\pi\gamma^3\big/3\Delta G_V^2\right)$ has been calculated for the formation of the various thermodynamically permissible phases over the temperature range 50–600 °C from a homogeneous supercooled liquid (as an approximate to the amorphous glass matrix), in the framework of CNT. The nearest-neighbour broken-bond model [75] (as implemented in the MatCalc software package) was used to estimate the interfacial energies (γ) for the different phases (Table 4), and the thermodynamic assessment was used to calculate the onset driving force for nucleation at the equilibrium composition for each phase, ΔG_V. The nearest-neighbour broken-bond model emphasises the chemical contribution to the interfacial energy, and although it does consider the density of bonds across the interface, it does not explicitly consider crystallographic misfits such as dislocations. While one may reasonably question the quantitative accuracy of such interfacial energy calculations for a crystal/crystal interface, it is expected that these estimates of interfacial energy are likely to be reasonable for crystals forming within an amorphous matrix.

Table 3
Comparison between the phase fractions observed in the *in situ* XRD experiment prior to melting and the values predicted by equilibrium thermodynamics (at 500 °C), showing an excellent agreement. Note that all samples reached their maximum crystallinity prior to melting, except $Al_{75}Ni_{15}Y_{10}$ which was ~90% crystalline at this stage.

Sample	Phase	Observed wt%	Calculated wt%
$Al_{87}Ni_9Y_4$	α-Al	45.0(4)	45.7
	Al_3Ni	9.7(2)	10.0
	$Al_{19}Ni_5Y_3$	45.3(4)	44.3
$Al_{86}Ni_{10}Y_4$	α-Al	39.3(4)	41.9
	Al_3Ni	14.8(2)	14.2
	$Al_{19}Ni_5Y_3$	44.9(5)	43.8
$Al_{83}Ni_{13}Y_4$	α-Al	30.2(6)	31.1
	Al_3Ni	27.9(3)	26.3
	$Al_{19}Ni_5Y_3$	42.0(5)	42.6
$Al_{81}Ni_{15}Y_4$	α-Al	23.4(4)	24.2
	Al_3Ni	36.4(4)	34.0
	$Al_{19}Ni_5Y_3$	40.3(5)	41.8
$Al_{75}Ni_{15}Y_{10}$	α-Al	7.6(6)	10.7
	Al_3Y	1.3(2)	4.5
	$Al_{19}Ni_5Y_3$	81.5(8)	84.8

Table 4
Estimates of the interfacial energies for the different phases relative to a liquid matrix based on the nearest-neighbour broken-bond model [75] (as implemented in MatCalc).

Sample	Interfacial energy relative to liquid at 300 °C (J/m^2)						
	Al_9Ni_2	α-Al	Al_3Y	Al_3Ni	$Al_{19}Ni_5Y_3$	$Al_{23}Ni_6Y_4$	Al_9Ni_3Y
$Al_{87}Ni_9Y_4$	0.114	0.083	0.274	0.197	0.161	0.117	0.141
$Al_{86}Ni_{10}Y_4$	0.114	0.082	0.276	0.198	0.163	0.119	0.142
$Al_{83}Ni_{13}Y_4$	0.115	0.076	0.282	0.200	0.168	0.124	0.148
$Al_{81}Ni_{15}Y_4$	0.114	0.070	0.284	0.202	0.172	0.128	0.151
$Al_{81}Ni_{15}Y_{10}$	0.103	0.026	0.306	0.198	0.184	0.142	0.161

Given the sensitivity of nucleation calculations to interfacial energy and the approximations made in estimating it using the broken bond model, the nucleation barrier (ΔG^*) calculations are made considering a range of ±10% for γ. The results of these calculations are shown in Fig. 16.

The Al_9Ni_3Y phase is predicted to have the lowest nucleation barrier for all of the samples at the temperatures where crystallisation occurs, whilst the Al_9Ni_2 and α-Al phases are predicted to have comparatively high barriers at the temperatures where they were observed to form experimentally. The Al_9Ni_3Y was never observed experimentally to be amongst the first phases forming from the glass and was actually the last phase to form from the amorphous matrix in the four compositions where it was observed.

In the $Al_{87}Ni_9Y_4$ and $Al_{86}Ni_{10}Y_4$ compositions (Figs. 4 and 6), α-Al is the first phase to crystallise from the glassy matrix appearing at ~180 °C and 220 °C, in the two alloy compositions, respectively. As can be seen from Fig. 16a, both the Al_9Ni_3Y and the $Al_{19}Ni_5Y_3$ phases are calculated to have significantly lower barriers to nucleation than α-Al (lower by a factor of 2–3 which then enters into an exponential of the CNT equation) at the temperatures corresponding to the first stage of crystallisation. One may question whether the α-Al has a large growth rate advantage compared to the Al_9Ni_3Y and the $Al_{19}Ni_5Y_3$ phases and this is the reason why it is the first phase to appear. However, at temperatures lower than ~300 °C, the α-Al is only 5–10 nm in size indicating limited scope for any advantage in growth to manifest itself in the competition. Furthermore, the calculated growth rates (assuming local equilibrium at the migrating interfaces) of the Al_9Ni_3Y and the $Al_{19}Ni_5Y_3$ phases are close to that of α-Al (both phases are ~50% of α-Al at 180 °C in $Al_{87}Ni_9Y_4$, and both phases are 60–75% of α-Al at 220 °C in $Al_{86}Ni_{10}Y_4$). This is a small growth rate advantage compared to the nucleation disadvantage of α-Al in the $Al_{87}Ni_9Y_4$ and $Al_{86}Ni_{10}Y_4$ compositions.

The SAXS results suggest the presence of a significant distribution of ~1 nm sized heterogeneities in the glassy matrix of the $Al_{87}Ni_9Y_4$ and $Al_{86}Ni_{10}Y_4$ compositions, and if these were Al-rich domains that could catalyse the formation of α-Al then this would represent a reasonable rationalisation for the observations reported here. Such heterogeneities would have to be present in a very large number density to lead to the large α-Al densities.

The $Al_{83}Ni_{13}Y_4$ and $Al_{81}Ni_{15}Y_4$ alloys, on the other hand, are more interesting. The first phase to form in the $Al_{83}Ni_{13}Y_4$ alloy is Al_9Ni_2 (at 270 °C), and in the $Al_{81}Ni_{15}Y_4$ alloy, both Al_9Ni_2 and Al_3Ni form together at 290 °C. CNT predicts that the Al_9Ni_2 phase has the highest barrier to nucleation of all thermodynamically permissible phases at the temperatures where it is observed to form experimentally (Fig. 16b and c) — in the $Al_{83}Ni_{13}Y_4$ alloy at 270 °C the calculated nucleation barrier for Al_9Ni_2 is ~0.75 eV and in the $Al_{81}Ni_{15}Y_4$ alloy at 290 °C, the barrier is over 3 eV. These are large barriers that would result in negligible nucleation according to CNT. On the other hand, the Al_3Ni phase which appears concurrently with Al_9Ni_2 as the first phases in the $Al_{81}Ni_{15}Y_4$ alloy at 290 °C has a
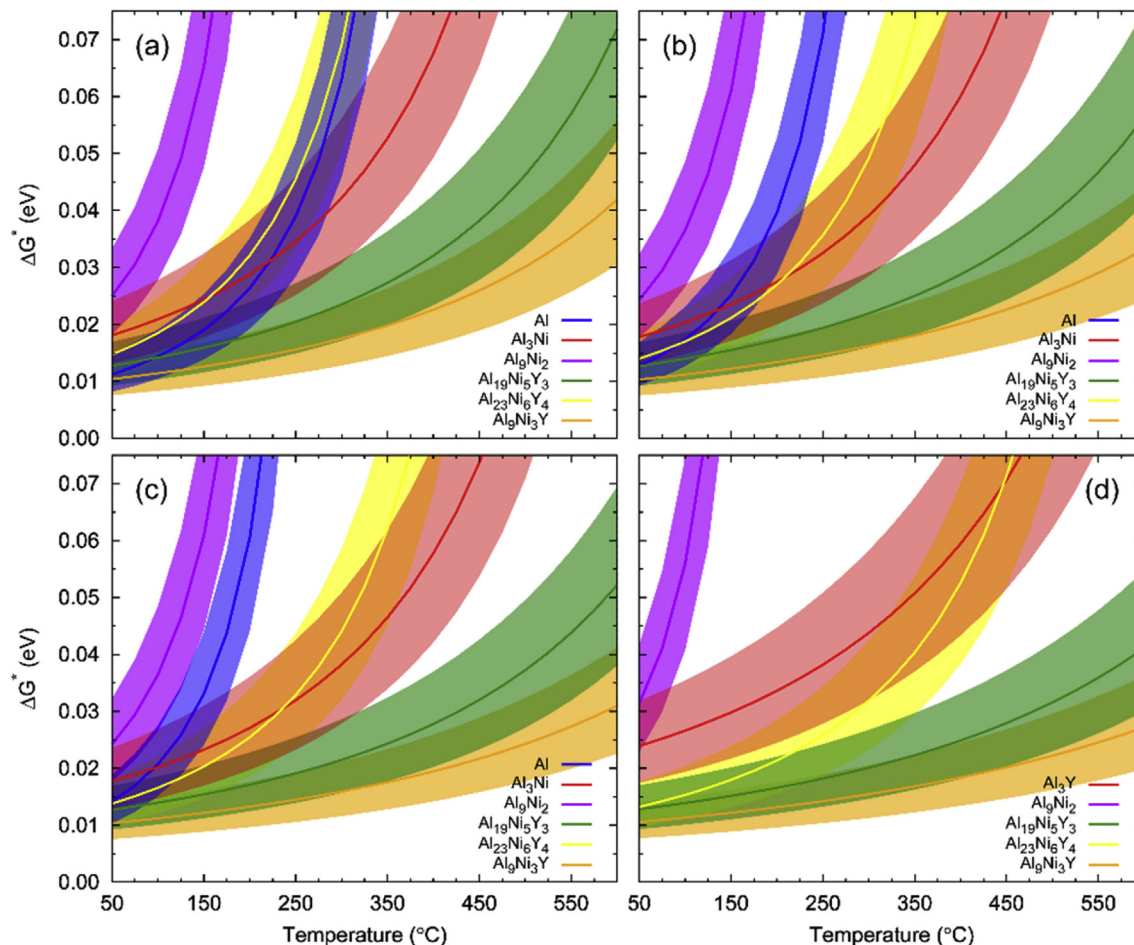
Fig. 16. Plots of the nucleation barrier (ΔG^*) verses temperature for phases in the Al-rich corner of the Al-Ni-Y phase diagram for the a) $Al_{87}Ni_9Y_4$, b) $Al_{83}Ni_{13}Y_4$, c) $Al_{81}Ni_{15}Y_4$, and d) $Al_{75}Ni_{15}Y_{10}$ alloys. The coloured bands represent ±10% margins on the interfacial energies estimated using the broken-bond model [75].

calculated nucleation barrier of ~0.038 eV (Fig. 16c). It is somewhat surprising to see two phases with calculated nucleation barriers of 3 eV and 0.038 eV appearing concurrently. Despite having the lowest calculated nucleation barriers, the Y containing intermetallics (Al_9Ni_3Y, $Al_{19}Ni_5Y_3$ and $Al_{23}Ni_6Y_4$) were never the first phases to form from the glass. Y is expected to be the slowest diffuser in this system in the amorphous matrix, and it is likely that the sluggish long range mass transfer required for the formation of the Y containing phases delays their nucleation, even though according to CNT they would be the first to form.

The common feature of the first forming Al_9Ni_2 phase in the $Al_{83}Ni_{13}Y_4$ alloy and the Al_9Ni_2 and Al_3Ni phases in the $Al_{81}Ni_{15}Y_4$ alloy is that these are the phases for which a thermodynamic driving force for formation exists but which require the least amount of long-range diffusion. The phases that nucleate first are those with compositions closest to the bulk composition, even if their barriers to nucleation calculated in the framework of CNT is the prohibitively high 3 eV. CNT does not even provide a qualitatively accurate description of the order of phases to appear from the glass.

These experimental observations and calculations support the suggestion by Kelton that long-range diffusional requirements must be incorporated into nucleation questions (coupled-flux models) [59,70–72]. The SAXS experiments on the glassy $Al_{83}Ni_{13}Y_4$ and $Al_{81}Ni_{15}Y_4$ alloys did not show the presence of any significant fractions of heterogeneities with different electron densities (i.e. Al-, Ni- or Y-rich regions) that may play a role in

catalysing the nucleation of high number densities of Al_9Ni_2 or Al_3Ni. The key is that these intermetallic phases may form in these compositions with only limited mass transport of Ni.

The _in situ_ experiments not only examined the phases that form during crystallisation from the glassy matrix, but also the competition in phase formation from the liquid during cooling from the melting temperature. The nucleation barrier plots shown in Fig. 16 predict very well the order of phases that form from the liquid during solidification, providing some confidence in the interfacial energy calculations in Table 4 and the driving forces calculated from the thermodynamic description. For example, in all of the alloys (with the exception of the $Al_{75}Ni_{15}Y_{10}$ alloy) the Al_9Ni_3Y phase forms rapidly during solidification from the melt, usually at the expense of the existing $Al_{19}Ni_5Y_3$. The Al_9Ni_3Y phase is the one predicted to have the lowest barrier to nucleation at the temperatures where solidification occurs during cooling. The $Al_{19}Ni_5Y_3$ phase, which does not melt completely at the temperatures investigated, maintains a fairly constant concentration on cooling. In the higher Ni concentration alloys, the Al_3Ni phase forms after Al_9Ni_3Y during solidification which is also in reasonably good agreement with the nucleation barriers shown in Fig. 16, bearing in mind the absence of the $Al_{23}Ni_6Y_4$ phase is to be expected given that the Y is already incorporated into the stable $Al_{19}Ni_5Y_3$ and Al_9Ni_3Y phases.

This comparison of the competition in phase formation from the glassy matrix and from the liquid during cooling clearly illustrates the critical role of long-range diffusion when considering the

competition in phase formation from the glass. The role of heterogeneities and medium-range order, as well as the need for long range diffusion in the solid glass (as emphasised by Kelton [70]), strongly influence the phases that form and their subsequent growth, and this can lead to the very large number densities of precipitates observed.

5. Conclusion

High-resolution, *in situ* synchrotron powder diffraction and quantitative Rietveld analysis has been used to study the competition in phase formation during the crystallisation of a range of Al-Ni-Y metallic glass alloys as they were continuously heated to melting and subsequently cooled. The FCC α-Al phase is the first to form in low Ni concentration alloys ($Al_{87}Ni_9Y_4$ and $Al_{86}Ni_{10}Y_4$) as part of a two-stage crystallisation process, while the Al_9Ni_2 intermetallic phase is the first to form in high Ni concentration alloys ($Al_{83}Ni_{13}Y_4$ and $Al_{81}Ni_{15}Y_4$), which crystallise via a three-stage process. For these four alloys, the partially disordered Al_9Ni_3Y phase was found to form preferentially over the $Al_{19}Ni_5Y_3$ phase upon cooling from the melt. In the case of the high Y concentration alloy, $Al_{75}Ni_{15}Y_{10}$, the $Al_{19}Ni_5Y_3$ phase was found to be more stable than the $Al_{23}Ni_6Y_4$ phase at low temperatures.

Quantitative phase analysis revealed that high concentrations of the Al_9Ni_2 phase form quickly during the first stage of crystallisation of high Ni alloys, particularly in the $Al_{83}Ni_{13}Y_4$ sample where over 60 wt% is observed. These measurements also showed that the second stage involves the formation of a considerable excess of the Al_3Ni phase (peaking at 65 wt% in the $Al_{81}Ni_{15}Y_4$ alloy) prior to the formation of the $Al_{19}Ni_5Y_3$ phase in the third stage. Analysis of the diffraction peak widths revealed that the α-Al and Al_9Ni_2 phases form with initial crystallite radii in the range of 5–10 nm which, when combined with their large concentrations, gives rise to crystallite number densities of $\sim 10^{23}$ m^{-3}. Laboratory SAXS measurements of the as-spun ribbons indicate that the low Ni concentration alloys contain nano-scale heterogeneities which may be responsible for the high number density of α-Al crystallites upon crystallisation. However, similar nano-scale heterogeneities were not observed in the high Ni concentration alloys.

The nucleation barriers for various phases were calculated by assuming a homogenous supercooled liquid and using a recent thermodynamic description of the Al-Ni-Y system. Interfacial energies were obtained using the nearest-neighbour broken-bond model. The results of these calculations show that the Al_9Ni_3Y phase should have the lowest barrier to nucleation, while the α-Al and Al_9Ni_2 phases should have among the highest barriers. While these calculations correctly predict the order of phases forming during solidification from the melt, they cannot accurately predict the formation of phases during crystallisation of the glass. Other effects, such as the kinetics of diffusion of different elements in the glassy matrix and pre-existing chemical heterogeneities must be considered.

References

[1] A.L. Greer, Metallic glasses, Science 267 (1995) 1947–1953.
[2] W.L. Johnson, Bulk glass-forming metallic alloys: science and technology, MRS Bull. 24 (1999) 42–56.
[3] A.L. Greer, E. Ma, Bulk metallic glasses: at the cutting edge of metals research, MRS Bull. 32 (2007) 611–619.
[4] Y. Li, S.J. Poon, G.J. Shiflet, J. Xu, D.H. Kim, J.F. Löffler, Formation of bulk metallic glasses and their composites, MRS Bull. 32 (2007) 624–628.
[5] W. Klement, R.H. Willens, P. Duwez, Non-crystalline structure in solidified gold–silicon alloys, Nature 187 (1960) 869–870.
[6] D. Turnbull, Under what conditions can a glass be formed? Contemp. Phys. 10 (1969) 473–488.
[7] A. Peker, W.L. Johnson, A highly processable metallic glass: Zr41.2Ti13.8-Cu12.5Ni10.0Be22.5, Appl. Phys. Lett. 63 (1993) 2342–2344.
[8] A. Inoue, Chapter 14 Bulk amorphous alloys, in: C. Suryanarayana (Ed.), Pergamon Mater. Ser., Pergamon, 1999, pp. 375–415.
[9] A.R. Yavari, J.J. Lewandowski, J. Eckert, Mechanical properties of bulk metallic glasses, MRS Bull. 32 (2007) 635–638.
[10] J. Eckert, J. Das, S. Pauly, C. Duhamel, Mechanical properties of bulk metallic glasses and composites, J. Mater. Res. 22 (2007) 285–301.
[11] Y. He, S.J. Poon, G.J. Shiflet, Synthesis and properties of metallic glasses that contain aluminum, Science 241 (1988) 1640–1642.
[12] A. Inoue, K. Ohtera, A.-P. Tsai, T. Masumoto, Aluminum-based amorphous alloys with tensile strength above 980 MPa (100 kg/mm2), Jpn. J. Appl. Phys. 27 (1988) L479.
[13] A. Inoue, K. Ohtera, K. Kita, T. Masumoto, New amorphous Mg-Ce-Ni alloys with high strength and good ductility, Jpn. J. Appl. Phys. 27 (1988) L2248.
[14] Y. He, G.M. Dougherty, G.J. Shiflet, S.J. Poon, Unique metallic glass formability and ultra-high tensile strength in Al-Ni-Fe-Gd alloys, Acta Metall. Mater. 41 (1993) 337–343.
[15] A. Inoue, Amorphous, nanoquasicrystalline and nanocrystalline alloys in Al-based systems, Prog. Mater. Sci. 43 (1998) 365–520.
[16] Q. Zheng, H. Ma, E. Ma, J. Xu, Mg–Cu–(Y, Nd) pseudo-ternary bulk metallic glasses: the effects of Nd on glass-forming ability and plasticity, Scr. Mater. 55 (2006) 541–544.
[17] D.G. Pan, W.Y. Liu, H.F. Zhang, A.M. Wang, Z.Q. Hu, Mg–Cu–Ag–Gd–Ni bulk metallic glass with high mechanical strength, J. Alloys Compd. 438 (2007) 142–144.
[18] A. Inoue, B.L. Shen, A.R. Yavari, A.L. Greer, Mechanical properties of Fe-based bulk glassy alloys in Fe–B–Si–Nb and Fe–Ga–P–C–B–Si systems, J. Mater. Res. 18 (2003) 1487–1492.
[19] A. Inoue, B.L. Shen, C.T. Chang, Super-high strength of over 4000 MPa for Fe-based bulk glassy alloys in [(Fe1−xCox)0.75B0.2Si0.05]96Nb4 system, Acta Mater. 52 (2004) 4093–4099.
[20] M.F. Ashby, A.L. Greer, Metallic glasses as structural materials, Scr. Mater. 54 (2006) 321–326.
[21] M.D. Archer, C.C. Corke, B.H. Harji, The electrochemical properties of metallic glasses,, Electrochim. Acta 32 (1987) 13–26.
[22] J.R. Scully, A. Gebert, J.H. Payer, Corrosion and related mechanical properties of bulk metallic glasses, J. Mater. Res. 22 (2007) 302–313.
[23] R. Jindal, V.S. Raja, M.A. Gibson, M.J. Styles, T.J. Bastow, C.R. Hutchinson, Effect of annealing below the crystallization temperature on the corrosion behavior of Al–Ni–Y metallic glasses, Corros. Sci. 84 (2014) 54–65.
[24] G.L. Makar, J. Kruger, Corrosion of magnesium, Int. Mater. Rev. 38 (1993) 138–153.
[25] K. Gusieva, C.H.J. Davies, J.R. Scully, N. Birbilis, Corrosion of magnesium alloys: the role of alloying, Int. Mater. Rev. 60 (2014) 169–194.
[26] J. Schroers, Processing of bulk metallic glass, Adv. Mater. 22 (2010) 1566–1597.
[27] W.L. Johnson, G. Kaltenboeck, M.D. Demetriou, J.P. Schramm, X. Liu, K. Samwer, C.P. Kim, D.C. Hofmann, Beating crystallization in glass-forming metals by millisecond heating and processing, Science 332 (2011) 828–833.
[28] R. Hasegawa, Present status of amorphous soft magnetic alloys, J. Magn. Magn. Mater. 215–216 (2000) 240–245.
[29] M. Vázquez, A. Hernando, A soft magnetic wire for sensor applications, J. Phys. Appl. Phys. 29 (1996) 939.
[30] W.L. Johnson, Is metallic glass poised to come of age? Nat. Mater. 14 (2015) 553–555.
[31] A. Inoue, N. Nishiyama, New bulk metallic glasses for applications as magnetic-sensing, chemical, and structural materials, MRS Bull. 32 (2007) 651–658.
[32] M. Chen, Mechanical behavior of metallic glasses: microscopic understanding of strength and ductility, Annu. Rev. Mater. Res. 38 (2008) 445–469.
[33] M.M. Trexler, N.N. Thadhani, Mechanical properties of bulk metallic glasses, Prog. Mater. Sci. 55 (2010) 759–839.

[34] D.C. Hofmann, J.-Y. Suh, A. Wiest, G. Duan, M.-L. Lind, M.D. Demetriou, W.L. Johnson, Designing metallic glass matrix composites with high toughness and tensile ductility, Nature 451 (2008) 1085–1089.

[35] D.C. Hofmann, J.-Y. Suh, A. Wiest, W. Johnson, New processing possibilities for highly toughened metallic glass matrix composites with tensile ductility, Scr. Mater. 59 (2008) 684–687.

[36] F.-F. Wu, K.C. Chan, S.-S. Jiang, S.-H. Chen, G. Wang, Bulk metallic glass composite with good tensile ductility, high strength and large elastic strain limit, Sci. Rep. 4 (2014).

[37] J. Eckert, J. Das, S. Pauly, C. Duhamel, Processing routes, microstructure and mechanical properties of metallic glasses and their composites, Adv. Eng. Mater. 9 (2007) 443–453.

[38] C.A. Schuh, T.C. Hufnagel, U. Ramamurty, Mechanical behavior of amorphous alloys, Acta Mater. 55 (2007) 4067–4109.

[39] Y. Yoshizawa, S. Oguma, K. Yamauchi, New Fe-based soft magnetic alloys composed of ultrafine grain structure, J. Appl. Phys. 64 (1988) 6044–6046.

[40] K. Suzuki, A. Makino, N. Kataoka, A. Inoue, T. Masumoto, High saturation magnetization and soft magnetic-properties of bcc Fe-Zr-B and Fe-Zr-B-M (M = transition-metal) alloys with nanoscale grain-size, Mater. Trans. Jim 32 (1991) 93–102.

[41] K. Takenaka, N. Nishiyama, A.D. Setyawan, P. Sharma, A. Makino, Performance of a prototype power transformer constructed by nanocrystalline Fe-Co-Si-B-P-Cu soft magnetic alloys, J. Appl. Phys. 117 (2015) 17D519.

[42] J.F. Löffler, J. Schroers, W.L. Johnson, Time–temperature–transformation diagram and microstructures of bulk glass forming Pd40Cu30Ni10P20, Appl. Phys. Lett. 77 (2000) 681–683.

[43] R. Busch, J. Schroers, W.H. Wang, Thermodynamics and kinetics of bulk metallic glass, MRS Bull. 32 (2007) 620–623.

[44] W. Yang, F. Liu, H. Liu, H.F. Wang, Z. Chen, G.C. Yang, Glass forming ability in Cu–Zr binary alloy: effect of nucleation mode, J. Alloys Compd. 484 (2009) 702–707.

[45] D.J. Browne, Z. Kovacs, W.U. Mirihanage, Comparison of nucleation and growth mechanisms in alloy solidification to those in metallic glass crystallisation — relevance to modeling, Trans. Indian Inst. Met. 62 (2010) 409–412.

[46] A. Wiest, G. Duan, M.D. Demetriou, L.A. Wiest, A. Peck, G. Kaltenboeck, B. Wiest, W.L. Johnson, Zr–Ti-based glasses optimized for high thermal stability and thermoplastic formability, Acta Mater. 56 (2008) 2625–2630.

[47] A. Inoue, K. Ohtera, A.-P. Tsai, T. Masumoto, New amorphous alloys with good ductility in Al-Y-M and Al-La-M (M=Fe, Co, Ni or Cu) systems, Jpn. J. Appl. Phys. 27 (1988) L280.

[48] A.L. Greer, New horizons for glass formation and stability, Nat. Mater. 14 (2015) 542–546.

[49] Y.K. Kim, J. Ryong Soh, D. Kyung Kim, H. Mo Lee, Glass formation in metallic Al–Ni–Y, J. Non-Cryst. Solids 242 (1998) 122–130.

[50] J.C. Foley, D.R. Allen, J.H. Perepezko, Analysis of nanocrystal development in Al-Y-Fe and Al-Sm glasses, Scr. Mater. 35 (1996) 655–660.

[51] N.C. Wu, M. Yan, L. Zuo, J.Q. Wang, Correlation between medium-range order structure and glass-forming ability for Al-based metallic glasses, J. Appl. Phys. 115 (2014) 43523.

[52] A.L. Vasiliev, M. Aindow, M.J. Blackburn, T.J. Watson, Phase stability and microstructure in devitrified Al-rich Al–Y–Ni alloys, Intermetallics 12 (2004) 349–362.

[53] Y.E. Kalay, C. Yeager, L.S. Chumbley, M.J. Kramer, I.E. Anderson, Initial crystallization in a nanostructured Al–Sm rare earth alloy, J. Non-Cryst. Solids 356 (2010) 1416–1424.

[54] J.E. Sweitzer, J.R. Scully, R.A. Bley, J.W.P. Hsu, Nanocrystalline Al87Ni8.7 Y 4.3 and Al90Fe5Gd5 alloys that retain the localized corrosion resistance of the amorphous state, Electrochem. Solid-State Lett. 2 (1999) 267–270.

[55] N.R. Tailleart, R. Huang, T. Aburada, D.J. Horton, J.R. Scully, Effect of thermally induced relaxation on passivity and corrosion of an amorphous Al–Co–Ce alloy, Corros. Sci. 59 (2012) 238–248.

[56] D.R. Allen, J.C. Foley, J.H. Perepezko, Nanocrystal development during primary crystallization of amorphous alloys, Acta Mater 46 (1998) 431–440.

[57] Y.J. Kim, R. Busch, W.L. Johnson, A.J. Rulison, W.K. Rhim, Experimental determination of a time–temperature-transformation diagram of the undercooled Zr41.2Ti13.8Cu12.5Ni10.0Be22.5 alloy using the containerless electrostatic levitation processing technique, Appl. Phys. Lett. 68 (1996) 1057–1059.

[58] J. Schroers, R. Busch, A. Masuhr, W.L. Johnson, Continuous refinement of the microstructure during crystallization of supercooled Zr41Ti14Cu12Ni10Be23 melts, Appl. Phys. Lett. 74 (1999) 2806–2808.

[59] K.F. Kelton, T.K. Croat, A.K. Gangopadhyay, L.-Q. Xing, A.L. Greer, M. Weyland, X. Li, K. Rajan, Mechanisms for nanocrystal formation in metallic glasses, J. Non-Cryst. Solids 317 (2003) 71–77.

[60] D.V. Louzguine-Luzgin, A. Inoue, Nano-devitrification of glassy alloys, J. Nanosci. Nanotechnol. 5 (2005) 999–1014.

[61] J. Antonowicz, M. Kędzierski, E. Jezierska, J. Latuch, A.R. Yavari, L. Greer, P. Panine, M. Sztucki, Small-angle X-ray scattering from phase-separating amorphous metallic alloys undergoing nanocrystallization, J. Alloys Compd. 483 (2009) 116–119.

[62] K.K. Sahu, N.A. Mauro, L. Longstreth-Spoor, D. Saha, Z. Nussinov, M.K. Miller, K.F. Kelton, Phase separation mediated devitrification of Al88Y7Fe5 glasses, Acta Mater. 58 (2010) 4199–4206.

[63] D.H. Kim, W.T. Kim, E.S. Park, N. Mattern, J. Eckert, Phase separation in metallic glasses, Prog. Mater. Sci. 58 (2013) 1103–1172.

[64] A.K. Gangopadhyay, T.K. Croat, K.F. Kelton, The effect of phase separation on subsequent crystallization in Al88Gd6La2Ni4, Acta Mater. 48 (2000) 4035–4043.

[65] R. Sabet-Sharghi, Z. Altounian, W.B. Muir, Formation, structure, and crystallization of Al-rich metallic glasses, J. Appl. Phys. 75 (1994) 4438–4441.

[66] A.P. Tsai, T. Kamiyama, Y. Kawamura, A. Inoue, T. Masumoto, Formation and precipitation mechanism of nanoscale Al particles in Al-Ni base amorphous alloys, Acta Mater. 45 (1997) 1477–1487.

[67] M.D.H. Lay, A.J. Hill, P.G. Saksida, M.A. Gibson, T.J. Bastow, 27Al NMR measurement of fcc Al configurations in as-quenched Al85Ni11Y4 metallic glass and crystallization kinetics of Al nanocrystals, Acta Mater. 60 (2012) 79–88.

[68] H.W. Sheng, Y.Q. Cheng, P.L. Lee, S.D. Shastri, E. Ma, Atomic packing in multicomponent aluminum-based metallic glasses, Acta Mater. 56 (2008) 6264–6272.

[69] Y.E. Kalay, I. Kalay, J. Hwang, P.M. Voyles, M.J. Kramer, Local chemical and topological order in Al–Tb and its role in controlling nanocrystal formation, Acta Mater. 60 (2012) 994–1003.

[70] K.F. Kelton, Time-dependent nucleation in partitioning transformations, Acta Mater. 48 (2000) 1967–1980.

[71] K.F. Kelton, Liquid structure and long range diffusion: their impact on glass formation and nanoscale devitrification, Intermetallics 14 (2006) 966–971.

[72] J. Diao, R. Salazar, K.F. Kelton, L.D. Gelb, Impact of diffusion on concentration profiles around near-critical nuclei and implications for theories of nucleation and growth, Acta Mater. 56 (2008) 2585–2591.

[73] W.J. Golumbfskie, S.N. Prins, T.J. Eden, Z.-K. Liu, Predictions of the Al-rich region of the Al–Co–Ni–Y system based upon first-principles and experimental data, Calphad 33 (2009) 124–135.

[74] W.J. Golumbfskie, Modeling of the Aluminum-rich Region of the Aluminum-cobalt-nickel-yttrium System via Computational and Experimental Methods for the Development of High Temperature Al-based Alloys (Ph.D. thesis), The Pennsylvania State University, 2005.

[75] B. Sonderegger, E. Kozeschnik, Generalized nearest-neighbor broken-bond analysis of randomly oriented coherent interfaces in multicomponent Fcc and Bcc structures, Metall. Mater. Trans. A 40 (2009) 499–510.

[76] K.S. Wallwork, B.J. Kennedy, D. Wang, The high resolution powder diffraction beamline for the Australian Synchrotron, in: J. Choi, S. Rah (Eds.), AIP Conf. Proc., Amer Inst Physics, Melville, 2007, pp. 879–882.

[77] A. Bergamaschi, A. Cervellino, R. Dinapoli, F. Gozzo, B. Henrich, I. Johnson, P. Kraft, A. Mozzanica, B. Schmitt, X. Shi, The MYTHEN detector for X-ray powder diffraction experiments at the Swiss Light Source, J. Synchrotron Radiat. 17 (2010) 653–668.

[78] H.P. Klug, L.E. Alexander, X-ray Diffraction Procedures for Polycrystalline and Amorphous Materials, second ed., Wiley, New York, 1974.

[79] M.R. Rowles, CONVAS2: a program for the merging of diffraction data, Powder Diffr. 25 (2010) 297–301.

[80] H.M. Rietveld, A profile refinement method for nuclear and magnetic structures, J. Appl. Crystallogr. 2 (1969) 65–71.

[81] R.J. Hill, C.J. Howard, Quantitative phase analysis from neutron powder diffraction data using the Rietveld method, J. Appl. Crystallogr. 20 (1987) 467–474.

[82] B.H. O'Connor, M.D. Raven, Application of the rietveld refinement procedure in assaying powdered mixtures, Powder Diffr. 3 (1988) 2–6.

[83] I.C. Madsen, N.V.Y. Scarlett, Quantitative phase analysis, in: R.E. Dinnebier, S.J.L. Billinge (Eds.), Powder Diffr., Royal Society of Chemistry, Cambridge, 2008, pp. 298–331 (Chapter 11).

[84] H. Chen, Y. He, G.J. Shiflet, S.J. Poon, Mechanical properties of partially crystallized aluminum based metallic glasses, Scr. Metall. Mater. 25 (1991) 1421–1424.

[85] R.J. Hill, I.C. Madsen, The effect of profile-step counting time on the determination of crystal structure parameters by X-ray Rietveld analysis, J. Appl. Crystallogr. 17 (1984) 297–306.

[86] A.J. Bradley, A. Taylor, The crystal structures of Ni2Al3 and NiAl3, Philos. Mag. 23 (1937) 1049–1067.

[87] R.E. Gladyshevskii, K. Cenzual, E. Parthé, The crystal structure of orthorhombic Gd3Ni5Al19, a new representative of the structure series R2+mT4+mAl15+4m, J. Solid State Chem. 100 (1992) 9–15.

[88] R.E. Gladyshevskii, K. Cenzual, H.D. Flack, E. Parthé, Structure of RNi3Al9 (R = Y, Gd, Dy, Er) with either ordered or partly disordered arrangement of Al-atom triangles and rare-earth-metal atoms, Acta Crystallogr. Sect. B 49 (1993) 468–474.

[89] R.E. Gladyshevskii, K. Cenzual, Structure of Y3TaNi6+xAl26: a filled-up substitution variant of the BaHg11 type, J. Alloys Compd. 240 (1996) 266–271.

[90] X.Z. Li, K.H. Kuo, Decagonal quasicrystals with different periodicities along the tenfold axis in rapidly solidified Al–Ni alloys, Philos. Mag. Lett. 58 (1988) 167–171.

[91] K.J. Blobaum, D. Van Heerden, A.J. Gavens, T.P. Weihs, Al/Ni formation reactions: characterization of the metastable Al9Ni2 phase and analysis of its formation, Acta Mater. 51 (2003) 3871–3884.

[92] A.M.B. Douglas, The structure of Co2Al9, Acta Crystallogr. 3 (1950) 19–24.

[93] R.E. Gladyshevskii, E. Parthé, Structure of monoclinic Y4Ni6Al23, Acta Crystallogr. Sect. C 48 (1992) 232–236.

[94] Y. Li, K. Georgarakis, S. Pang, J. Antonowicz, F. Charlot, A. LeMoulec, T. Zhang, A.R. Yavari, AlNiY chill-zone alloys with good mechanical properties, J. Alloys Compd. 477 (2009) 346–349.

[95] D. Balzar, N. Audebrand, M.R. Daymond, A. Fitch, A. Hewat, J.I. Langford, A. Le Bail, D. Louër, O. Masson, C.N. McCowan, N.C. Popa, P.W. Stephens, B.H. Toby, Size—strain line-broadening analysis of the ceria round-robin sample, J. Appl. Crystallogr. 37 (2004) 911—924.

[96] F. De Geuser, A. Deschamps, Precipitate characterisation in metallic systems by small-angle X-ray or neutron scattering, Comptes Rendus Phys. 13 (2012) 246—256.

[97] R. Jindal, Study of Structure-corrosion Property Correlations in Three Al-Y-Ni Based Metallic Glasses (Ph.D. thesis), Indian Institute of Technology and Monash University, 2015.

[98] C. Zener, Theory of growth of spherical precipitates from solid solution, J. Appl. Phys. 20 (1949) 950—953.